fibers

MDPI

Article

Synthesis and Characterization of Keratin-Based Scaffold for Potential Tissue Engineering Applications

Murugiah Krishani [1,*], Jia Ning Chong [1], Wan Rong Lim [1], Norwahyu Jusoh [2], Nonni Soraya Sambudi [3] and Hazwani Suhaimi [1,*]

[1] Faculty of Integrated Technologies, Universiti Brunei Darussalam, Jalan Tungku Link, Gadong BE1410, Brunei; 21b4009@ubd.edu.bn (J.N.C.); 20b4028@ubd.edu.bn (W.R.L.)
[2] Chemical Engineering Department, Universiti Teknologi PETRONAS, Bandar Seri Iskandar 32610, Perak, Malaysia; norwahyu.jusoh@utp.edu.my
[3] Department of Chemical Engineering, Universitas Pertamina, Simprug, Jakarta 12220, Indonesia; nonni.ss@universitaspertamina.ac.id
* Correspondence: 20h8400@ubd.edu.bn (M.K.); hazwani.suhaimi@ubd.edu.bn (H.S.)

Highlights

What are the main findings?

- Physicochemical characterization, surface morphology analysis, and tensile strength testing of the fabricated Keratin-Gelatin (KG) and Keratin-Gelatin-Hydroxyapatite (HAp) (KGH) scaffolds demonstrated promising results for tissue engineering applications.
- Specifically, the KGH scaffold exhibited higher cell viability compared to the KG scaffold, highlighting the potential of the HAp-enriched scaffold as a promising candidate for bone regeneration.

What is the implication of the main finding?

- The potential of human nail-derived keratin and HAp as promising biomaterials for tissue engineering scaffolds.
- The use of human nail waste as a keratin source and marine shell waste for HAp supports the principles of a circular economy, promoting sustainable and value-added reuse of biological waste materials.

Abstract

Keratin, a fibrous structural protein, has been employed as a biomaterial for hemostasis and tissue repair due to its structural stability, mechanical strength, biocompatibility, and biodegradability. While extensive research has focused on developing scaffolds using keratin extracted from various sources, no studies to date have explored the use of keratin derived from human nail clippings. In this study, keratin was extracted from human nail clippings using the Shindai method and used to fabricate and compare two types of scaffolds for bone tissue engineering via the freeze-drying method. The first scaffold consisted of keratin combined with gelatin (KG), while the second combined keratin, gelatin, and hydroxyapatite (HAp) (KGH), the latter synthesized from blood cockle clam shells using the wet precipitation method. Physicochemical characterization and surface morphology analysis of keratin and both scaffolds showed promising results. Tensile strength testing revealed a significant difference in Young's modulus. The KG scaffold exhibited higher porosity, water uptake, and water retention capacity compared to the KGH scaffold. In vitro biocompatibility studies revealed that the KGH scaffold supported higher cell proliferation compared to the KG scaffold. This study demonstrates the potential of using human nail-derived keratin in composite scaffold fabrication and serves as a foundation for future research on this novel biomaterial source.

check for updates

Academic Editor: Martin J. D. Clift

Received: 11 June 2025
Revised: 9 July 2025
Accepted: 14 July 2025
Published: 17 July 2025

Citation: Krishani, M.; Chong, J.N.; Lim, W.R.; Jusoh, N.; Sambudi, N.S.; Suhaimi, H. Synthesis and Characterization of Keratin-Based Scaffold for Potential Tissue Engineering Applications. *Fibers* **2025**, *13*, 97. https://doi.org/10.3390/fib13070097

Copyright: © 2025 by the authors. Licensee MDPI, Basel, Switzerland. This article is an open access article distributed under the terms and conditions of the Creative Commons Attribution (CC BY) license (https://creativecommons.org/licenses/by/4.0/).

Keywords: keratin; gelatin; hydroxyapatite; scaffold; human nail clipping; blood cockle clam; freeze drying; wet precipitation; biomaterial; bone tissue engineering

1. Introduction

Bone tissue plays a crucial role in maintaining the body's structure by providing mechanical support, protection, mineral homeostasis, endocrine regulation, and hematopoiesis. However, conditions such as osteoporosis, bone cancer, inflammatory diseases, infections, and Paget's disease can compromise bone integrity [1]. While bone tissue has a natural ability to heal, severe fractures may require bone grafts when self-repair is insufficient. Bone grafts are essential for addressing bone deficiencies, particularly in cases where conventional treatments like radiation therapy, chemotherapy, and drug delivery systems prove ineffective against certain cancer types that result in substantial bone loss [2].

Tissue engineering (TE) involves combining cells, scaffolds, and signaling molecules to create three-dimensional (3D) constructs that repair or restore tissue function. When applied to bone repair, this approach is known as bone tissue engineering (BTE). In BTE, scaffolds serve as the foundation for cell attachment and growth factor delivery, supporting tissue regeneration. Ideally, scaffolds should be biodegradable, mechanically robust, and highly porous, allowing osteogenic cells to migrate and initiate new bone formation. Additionally, bone scaffolds must exhibit key properties such as biocompatibility, controlled degradability, and mechanical stability without triggering an immune response [3,4].

Bone scaffolds can be made from three primary material categories: polymers (both biopolymers and synthetic polymers), ceramics, and metals. Additionally, composite materials, formed by combining two or more components, offer enhanced biomechanical and biocompatibility properties [5]. Among these, biopolymers are particularly promising for artificial bone production due to their excellent biocompatibility, ease of fabrication, and lower cost compared to metals and ceramics [6,7].

Despite advancements in technologies aimed at restoring damaged tissues and organs, the host response to biomaterial implantation remains a significant challenge in regenerative medicine. The innate and adaptive immune systems play a crucial role in this response, forming the interface between the scaffold and host inflammation. These cellular and molecular interactions ultimately determine implant success and tissue regeneration [8]. One approach to mitigating immune rejection is the use of human-derived materials, which are recognized as "self" by the immune system and are less likely to trigger an adverse response. Building on this concept, the present work aims to develop a scaffold using keratin extracted from human nail clippings for the treatment of bone defects.

Keratin is a fibrous biopolymer naturally found in hair, nails, horns, feathers, wool, and hooves. Its high cysteine content contributes to the formation of strong disulfide crosslinks, giving keratin notable mechanical strength and chemical stability [9–11]. It exists in two main forms—soft and hard keratin—distinguished by their sulfur content and structural roles. Hard keratin, abundant in nails and hair, has been widely studied for biomaterial applications due to its superior durability and biocompatibility [12–16]. Structurally, keratin can be categorized into alpha-keratin (in mammals) and beta-keratin (in birds and reptiles), each featuring nanoscale filament-matrix architectures. These structures, stabilized by disulfide, hydrogen, and ionic bonds, make keratin insoluble in most solvents and resistant to enzymatic degradation [17–23]. Rich in amino acids like glycine, serine, and cysteine, keratin demonstrates favorable biological interactions and stability, making it suitable for regenerative applications. Keratin's bioactivity, self-assembly capacity, and compatibility with various processing methods allow it to be fabricated into hydrogels, sponges, fibers,

and films for wound healing and tissue engineering [22,23]. Several keratin-based scaffolds have shown promise in bone tissue engineering, especially when combined with other biomaterials such as collagen, chitosan, or hydroxyapatite (HAp), enhancing mechanical strength, bioactivity, and osteoinductivity [24].

Despite extensive use of keratin from hair, wool, and feathers, keratin derived from human nail clippings remains unexplored. Given the similar protein composition between hair and nails [25,26] and the continuous growth of fingernails, nail clippings represent a renewable and sustainable keratin source [27]. The majority of previous research on keratin scaffolds has utilized keratin derived from hair, wool, or feathers; nevertheless, nail keratin possesses unique characteristics that could benefit bone scaffolds. Cell-binding motifs are abundant in hair and wool (mammalian α-keratin), which have been employed extensively in biomaterials. Wool/hair keratin fibers, for instance, have exposed peptide sequences that promote hemostasis and cell adhesion. Bird keratin, or β-keratin, is stronger on a weight-per-weight basis and has a distinct structure (pleated β-sheets vs. coiled α-helices). Human nail keratin is α-keratin, just like hair, but it has a special composition and is incredibly hard. Human hair has a higher percentage of softer keratins, while human nails have about 80% hard α-keratin (and 20% soft keratin). Thus, the density of cystine (disulfide) crosslinks is higher in nail keratin. The toughness of the nail plate is, in fact, specifically assigned to its "high proportions of cystine resulting in large numbers of disulfide cross-links". In general, the sulfur-rich amino acids that hold nail keratin's fibers together are more numerous. Mechanical and chemical resistance are imparted by the high cysteine content of keratin, which is maximized in nails [28,29].

This study utilizes the Shindai method [30] to extract keratin from nail clippings and incorporates it into a composite scaffold with gelatin and HAp to overcome keratin's mechanical limitations, addressing both regenerative efficacy and immune compatibility. The Shindai method is specifically designed and described to extract high-purity, structurally intact keratins that can be used to fabricate bone scaffolds. It provides a greater yield, a wider recovery of functional subunits, and softer conditions that maintain protein functionalities essential for scaffold performance when compared to traditional Sodium Dodecyl Sulfate (SDS) and Dithiothreitol (DTT) methods [30].

Gelatin, a naturally derived biopolymer from collagen, is widely used in biomedical and tissue engineering applications due to its biocompatibility, biodegradability, and cost-effectiveness [31–33]. It is commonly employed in medical products such as wound dressings, surgical pads, and adhesives [34–36]. Gelatin provides cell-binding sites essential for cell attachment and proliferation. Despite its many advantages, its inherent mechanical weakness limits standalone applications [37–39]. To address this, studies have shown that blending gelatin with polymers or bioactive materials, such as chitosan or HAp, enhances its structural and biological performance. Notably, gelatiN–HAp composites have demonstrated improved mechanical strength and osteoconductivity, making them promising candidates for bone scaffold development [40,41].

HAp, with the formula $Ca_{10}(PO_4)_6(OH)_2$, is widely used in bone regeneration due to its close chemical resemblance to the mineral component of human bone and its excellent biocompatibility [42,43]. Its incorporation into scaffolds enhances bioactivity and promotes osteoblast development and proliferation [44]. HAp can be synthesized from various calcium-rich natural sources such as egg shells, clam shells, fish scales, and animal bones. In this study, HAp was synthesized from blood cockle clam shells using the wet precipitation method, a simple and effective approach [45].

Therefore, this work aims to develop two types of keratin-based scaffolds: (1) a keratin–gelatin scaffold (KG) and (2) a keratin–gelatin–HAp scaffold (KGH). Human nail clippings were used as a sustainable source of keratin, extracted using the Shindai method. Com-

mercial bovine gelatin was incorporated to enhance biocompatibility, while synthesized HAp improved mechanical strength and osteoconductivity. To preserve the biological activity of heat-sensitive materials like keratin, scaffold fabrication was performed using the freeze-drying (lyophilization) technique [46]. Chemical and structural characterization of the extracted keratin, synthesized HAp, and fabricated scaffolds were conducted using Fourier transform infrared spectroscopy (FTIR), X-ray diffraction (XRD), scanning electron microscopy (SEM), and energy-dispersive X-ray spectroscopy (EDX). Additional analyses included the evaluation of scaffold porosity, tensile strength, water uptake, and water retention. As a highly vascularized hard tissue, bone undergoes continuous remodeling throughout life through the coordinated actions of osteoblasts and osteoclasts, which facilitate bone formation and resorption [47]. To assess the biocompatibility of the scaffolds, a cell proliferation study was conducted using the human osteoblast (HOB) cells. This work is significant because it exhibits a circular economy strategy: recycling marine shells and nail keratin not only reduces landfill trash and the environmental impact, but it also produces valuable biomaterials. This is consistent with regenerative medicine's increasing need for bio-derived, sustainable scaffolds.

2. Materials and Methods

2.1. Materials

Human nail clippings were collected from healthy volunteers in accordance with approved standard operating procedures. Blood cockle clam shells were obtained from a local fish market in Brunei, while bovine gelatin was purchased from a local grocery store. HOB cells were purchased from PromoCell GmbH, Heidelberg, Germany. Ethanol, chloroform, methanol, thiourea, urea, 2-mercaptoethanol, hydrochloric acid, sodium hydroxide (NaOH), orthophosphoric acid (H_3PO_4), and trypan blue were purchased from Merck (Darmstadt, Germany). Tris base (tris(hydroxymethyl)aminomethane) and lead acetate were obtained from BIO-RAD (Hercules, CA, USA) and Merck (Mumbai, India), respectively. Dulbecco's modified eagle medium (DMEM), fetal bovine serum (FBS), non-essential amino acids (NEAA), trypsin–ethylenediaminetetraacetic acid (EDTA), and phosphate-buffered saline (PBS) were purchased from Fisher Scientific Ltd. (Loughborough, UK). All reagents were of analytical grade and used as received without further purification.

2.2. Keratin Extraction

Collected human nail clippings were initially washed several times with distilled water and ethanol to remove surface contaminants. The cleaned clippings were then immersed in a chloroform–methanol solution (2:1, v/v) for 24 h to remove surface lipids. Following delipidation, the clippings were rinsed with reverse osmosis water and air-dried overnight to allow complete evaporation of residual solvents.

Keratin extraction buffer was prepared by mixing 25 mM tris base (tris(hydroxymethyl) aminomethane), 2.6 M thiourea, 5 M urea, and 5% (v/v) 2-mercaptoethanol in distilled water. The pH of the buffer was adjusted to 8.5 using 8M hydrochloric acid. A total of 60 g of delipidized nail clippings was added to 1 L of the prepared extraction buffer. The mixture was stirred for approximately 3 min and then incubated in an oven at 50 °C for 72 h. Every 12 h, the solution was manually stirred to enhance extraction efficiency.

After the incubation period, the mixture was filtered using Whatman filter paper (Cytiva, Maidstone, UK) to separate the solubilized proteins from the solid residues. The resulting filtrate was centrifuged at 15,000$\times$ g for 20 min at room temperature to remove residual particulates. The supernatant was dialyzed against distilled water using a dialysis membrane with a molecular weight cut-off of 3.5 kDa for seven days, with the external water replaced daily. During dialysis, the protein solution gradually turned milky white,

indicating protein polymerization and aggregation. The dialyzed protein solution was subsequently frozen at −86 °C for 48 h and then subjected to freeze-drying using a lyophilizer at −48 °C and 3.5 Pa for another 48 h. The final product, keratin in powdered form, was collected and stored for further analysis [25].

To confirm the presence of keratin, 2 mL of the protein solution was mixed with 2 mL of 40% (*v*/*v*) NaOH solution in a test tube. The mixture was boiled over a flame for one minute, then cooled under running tap water. Five drops of lead acetate were added, and the formation of a black or brown precipitate confirmed the presence of keratin protein [48].

2.3. Hydroxyapatite Synthesis

HAp used in this study was synthesized from blood cockle clam shells using the wet precipitation method, as previously reported by Murugiah et al. [45], explained briefly as follows. Blood cockle clam shells collected from the local fish market were thoroughly cleaned with distilled water and oven-dried at 110 °C for 1 h. The dried shells were then crushed into a fine powder using a mortar and pestle. The resulting powder was calcined at 900 °C for 3 h to obtain calcium oxide. A 1M solution of the calcined clam shell powder was prepared by mixing it with distilled water and stirring vigorously for 1 h using a magnetic stirrer to ensure homogeneity. Subsequently, the calcium-containing solution was titrated with 0.6M H_3PO_4 at room temperature under continuous stirring. The titration proceeded until all the H_3PO_4 was added, while the pH of the mixture was monitored using a digital pH meter. The final pH was adjusted to 10 by the dropwise addition of 1M NaOH. The resulting suspension was then aged at room temperature for 24 h to allow the formation of a supersaturated HAp suspension. The resulting HAp was filtered to remove excess water and subsequently dried in an oven at 110 °C. The dried powder was then sintered at 900 °C for 1 h with a heating rate of 5 °C/min to obtain crystalline HAp. The synthesized HAp was then incorporated into the fabrication of the KGH scaffold in the present study.

2.4. Scaffold Fabrication

2.4.1. Fabrication of Keratin–Gelatin Scaffold

A total of 2.6 g of bovine gelatin was dissolved in 100 mL of hot water at approximately 70 °C. From this solution, 32 mL was mixed with 16 mL of 3% (*v*/*v*) keratin protein solution, resulting in a total volume of 48 mL. The mixture was homogenized using a homogenizer for 5 h to ensure uniformity. After homogenization, the solution was poured into a mold and frozen overnight at −86 °C. The following day, the frozen mixture was subjected to freeze-drying in the lyophilizer for 48 h. Preliminary trials and practical considerations including solution viscosity, gelation behavior, and scaffold integrity throughout the lyophilization process were used to define this composition.

Keratin's high sulfur content, excellent biocompatibility, and inherent mechanical rigidity led to its selection as the main biomaterial at 3% (*w*/*v*). This concentration offered adequate structural integrity without causing problems with mixing or solubility. Gelatin was added in a relatively small quantity (2.6% *w*/*v*) to enhance cell adhesion, flexibility, and hydrophilicity—properties that keratin by itself is deficient in. Additionally, the creation of consistent scaffold shape and porosity was facilitated by gelatin.

2.4.2. Fabrication of Keratin–Gelatin–Hydroxyapatite Scaffold

A gelatin solution was prepared following the same procedure used for the KG scaffold. Separately, a 3% (*w*/*v*) HAp solution was prepared by dispersing HAp powder in distilled water and homogenizing the mixture for 1 h. Subsequently, 32 mL of the prepared gelatin solution was mixed with 16 mL of a combined 3% (*v*/*v*) HAp and 3% (*v*/*v*) keratin solution, resulting in a final volume of 48 mL. The resulting mixture was homogenized for 5 h to ensure uniform dispersion of all components. After homogenization, the solution

was poured into a mold and frozen overnight at −86 °C. The following day, the frozen composite was freeze-dried using the lyophilizer for 48 h.

Our selection of 3% HAp guarantees a sufficient mineral content to encourage osteointegration while maintaining the flexibility of the scaffold and preventing brittleness. Due to its natural bioactivity and capacity to promote mineral deposition, a 3% keratin concentration was used. Furthermore, adding about 2.6% gelatin improves cell adhesion and structural cohesiveness without sacrificing mechanical integrity. With a scaffold with balanced mechanical characteristics (compressive strength in the MPa range, porosity > 70%) and strong biological performance, including support for osteoblast viability and extracellular matrix formation, this formulation satisfies the requirements for efficient cancellous bone substitutes.

2.5. Characterization Techniques

2.5.1. Functional Group Analysis

Keratin, KG, and KGH scaffolds were chemically characterized using a Shimadzu IRAffinity-1 FTIR spectrophotometer (Shimadzu Corporation, Kyoto, Japan). Spectral data were collected in the range of 4000 cm^{-1} to 400 cm^{-1} to identify functional groups and confirm the presence of characteristic chemical bonds.

2.5.2. Crystallinity Analysis

XRD analysis was performed to evaluate and compare the crystalline structures of keratin, KG, and KGH scaffolds using an Aeries benchtop X-ray diffractometer (Malvern Panalytical, Almelo, The Netherlands). The analysis was conducted using Cu Kα radiation, and diffraction patterns were recorded over a 2α range of 10–80°.

2.5.3. Surface Morphology

The surface morphology of keratin, KG, and KGH scaffolds was examined using a JEOL JSM-7600F field emission scanning electron microscope operated at an accelerating voltage of 5 kV (JEOL Ltd., Tokyo, Japan). Samples were prepared by mounting them directly onto aluminum stubs using conductive adhesive tape. ImageJ (version 1.54g) software was used to analyze the average pore size of the KG and KGH scaffolds. The SEM images were imported into the software, and the threshold was adjusted to isolate pore regions, highlighted in red. Particle analysis was then conducted to calculate the average pore size [49]. Elemental analysis of the keratin extract, KG, and KGH scaffolds was conducted using EDX integrated with the SEM.

2.5.4. Water Uptake Capability and Water Retention Capability

To evaluate the water uptake and retention capabilities, scaffold samples were first weighed to obtain their initial dry weight. The samples were then immersed in distilled water in a beaker for 24 h at room temperature. After immersion, the scaffolds were removed, gently blotted with filter paper to remove surface water, and weighed to determine their wet weight.

For water retention analysis, the hydrated scaffold samples were placed into centrifuge tubes and centrifuged at 500 rpm for 3 min. Immediately after centrifugation, the samples were weighed again to determine the retained water content [50].

The water uptake and water retention capabilities were calculated using Equation (1) and Equation (2), respectively:

$$\frac{W_w - W_d}{W_d} \times 100 \quad (1)$$

$$\frac{W_w^t - W_d}{W_d} \times 100 \quad (2)$$

where W_d is the dry weight of the scaffold; W_w is the wet weight after immersion; and W_w^t is the weight after centrifugation.

2.5.5. Porosity

The porosity (Ø) of the scaffolds was determined using the liquid displacement method, with ethanol serving as the displacement liquid due to its ability to penetrate pores without causing scaffold swelling. Each scaffold was cut into three smaller pieces, and the dimensions (length, width, and height) of each piece were measured to calculate the scaffold volume (Vs). The dry weight (W_d) of each scaffold piece was recorded prior to immersion. Each scaffold piece was then individually immersed in 30 mL of ethanol in an Erlenmeyer flask. The flask was attached to a vacuum pump and subjected to vacuum for 5 min while covered to facilitate ethanol infiltration into the scaffold pores by removing trapped air bubbles. After vacuuming, the scaffold was carefully removed, blotted with filter paper to remove excess ethanol, and weighed to obtain the wet weight (W_w). The scaffold porosity was calculated using Equation (3) [25]:

$$\frac{Vp}{Vs} \times 100 = \frac{W_w - W_d}{\rho_e \times Vs} \times 100 \quad (3)$$

where Vp is the pore volume, and ρ_e is the density of ethanol.

2.5.6. Tensile Strength Testing

The KG and KGH scaffolds were cut into rectangular strips measuring 9 cm in length and 2 cm in width. Tensile strength tests were performed using a universal testing machine (INSTRON model 1405, Instron, Norwood, MA, USA) at an extension rate of 1 mm/min. The stress–strain curve obtained from the test was used to calculate the Young's modulus of both scaffold types [49].

2.6. Biocompatibility Study

2.6.1. Experimental Setup

For the cell viability investigation, the experiment was conducted over five days using a 24-well plate with three different setups: a 2D culture system, a 3D system with the KG scaffold, and a 3D system with the KGH scaffold. In the 3D system, the culture medium contained both the scaffold and seeded cells, whereas the 2D system consisted only of the culture medium and cells. The 2D setup was used exclusively for the trypan blue assay and served as the control. Manual cell counting for the trypan blue assay was performed on cells collected from the designated wells at the end of the 1st, 3rd, and 5th days of culture.

2.6.2. Scaffold Preparation

The scaffolds were sterilized by exposing both sides to ultraviolet (UV) light for eight hours. Following sterilization, they were stored in sterile vacuum-sealed plastic bags until use in cell culture experiments. To minimize the risk of cross-contamination, the sealed scaffold bags were further sterilized with 70% ethanol. Prior to cell culture, the scaffolds were soaked in 70% ethanol for 10 min and subsequently rinsed twice with PBS to remove any residual ethanol [51].

2.6.3. Cell Culture and Seeding

HOB cells were cultured in DMEM supplemented with 10% FBS and 2% NEAA at 37 °C in a humidified incubator containing 5% CO_2 and 95% air. The culture medium was replaced every two days. For subculturing, HOB cells were detached using a 0.25% trypsin and 0.1% EDTA solution, then resuspended in fresh DMEM [52]. Prior to cell seeding, the KG and KGH scaffolds were pre-soaked in their respective culture medium for at least

24 h to enhance hydrophilicity. For the 3D culture setup, scaffolds placed in a 24-well plate were seeded with 1 mL of the HOB cell suspension, containing 3.4×10^4 cells per well. As a control (2D system), the same volume of cell suspension was added to wells without scaffolds. All plates were kept in the humidified incubator at 37 °C, with media replacement every two days.

2.6.4. Cell Proliferation Assay

For cell proliferation assessment, HOB cells were seeded onto sterile disk-shaped portions of the composite scaffolds placed in 24-well plates. At designated time points, cells were detached from the scaffolds—or from the well surface in the case of control (2D) wells—using a trypsin solution. The scaffolds were then rinsed with complete DMEM to collect any remaining cells and subsequently removed from the wells. Trypsin activity in each well was neutralized with the same complete medium. The resulting cell suspensions were centrifuged at $300\times$ g for 5 min, and the cell pellets were resuspended in PBS. Trypan blue dye exclusion was used to distinguish live from dead cells. Manual cell counting was performed using a hemocytometer under a microscope at 24, 72, and 120 h (days 1, 3, and 5) [51].

2.6.5. Trypan Blue Assay

For manual cell counting using the trypan blue method, an equal volume of cell suspension and trypan blue dye was mixed in a microfuge tube. The mixture was then transferred to the hemocytometer, and a cover slip was carefully placed over the counting chamber. The hemocytometer was positioned on the microscope stage, and cells were counted within the central square and the four corner squares of the grid. Viable (living) cells appeared clear, whereas nonviable (dead) cells took up the blue dye [51]. Equations (4)–(7) were used to determine cell concentration.

The percentage of viable cells was calculated using Equation (4):

$$Viable\ cells\ (\%) = \frac{Number\ of\ viable\ cells}{Total\ number\ of\ cells} \times 100 \tag{4}$$

To obtain a representative cell count, the average number of viable cells per square was determined using Equation (5):

$$Average\ viable\ cells\ per\ square = \frac{Number\ of\ viable\ cells}{Number\ of\ squares\ counted} \tag{5}$$

The dilution factor was calculated based on the ratio of the total volume of the cell-dye mixture to the volume of the original cell suspension using Equation (6):

$$Dilution\ factor\ (DF) = \frac{Final\ volume}{Volume\ of\ cell\ suspension} \tag{6}$$

Finally, the viable cell concentration (cells/mL) in the original sample was determined using Equation (7) below:

$$Cell\ concentration\left(\frac{cells}{mL}\right) = Average\ viable\ cells\ per\ square \times DF \times 10^4 \tag{7}$$

The factor 10^4 accounts for the volume beneath each square of the hemocytometer, which is 0.0001 mL.

2.7. Statistical Analysis

All experiments were conducted using a minimum of three independent samples ($n \geq 3$). Results are presented as the mean ± standard deviation (SD). Statistical analysis was conducted using one-way analysis of variance (ANOVA) with a 95% confidence interval. For $n \geq 3$, error bars in the graphs represent ± SD [50].

3. Results and Discussions

3.1. Confirmatory Test for Keratin Protein

The formation of a black precipitate indicates the presence of keratin protein [48]. This occurs because the sulfur atoms from cysteine are converted to inorganic sodium sulfide under alkaline and heat conditions, which subsequently reacts with lead ions to form black lead sulfide, confirming the presence of keratin protein. The appearance of black precipitate was shown in Figure 1.

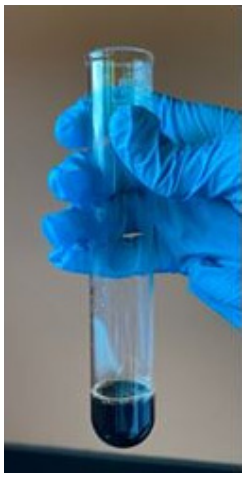


Figure 1. Confirmatory test for keratin protein.

3.2. FTIR Analysis

Accurate identification of individual component IR absorption peaks in composite scaffolds can be challenging due to overlapping bands arising from multiple chemical constituents [53]. Nevertheless, the characteristic functional groups present in keratin extracted from human nail clippings, HAp synthesized from blood cockle clam shells, as well as in the KG and KGH scaffolds, are identified and summarized below. In general, the Amide I–III bands are crucial for assessing protein conformation and structural changes in the protein backbone. The Amide I band, attributed to C=O stretching vibrations, appears as a strong transmission band between 1700 and 1600 cm^{-1}. The Amide II band, observed within the range of 1580–1540 cm^{-1}, corresponds to N–H bending and C–H stretching vibrations. The Amide III band, typically found between 1300 and 1220 cm^{-1}, results from C–N stretching and N–H bending, with additional contributions from C=O bending and C–C stretching. Amide I is associated with both α-helix and β-sheet secondary structures [54,55], while Amide III is predominantly linked to β-sheet structures [56].

The FTIR spectra of the extracted keratin, KG scaffold, and KGH scaffold are shown in Figure 2. A broad peak at 3278 cm^{-1} confirms N–H stretching, while the band at 2964 cm^{-1} indicates CH_3 stretching vibrations. The Amide I band (C=O stretching) is clearly observed at 1651 cm^{-1}, and the Amide II band (N–H bending and C–H stretching) appears at 1540 cm^{-1}. A peak at 1247 cm^{-1} confirms the presence of the Amide III band, corresponding to C–N stretching, N–H bending, and contributions from C=O bending and C–C stretching [57,58].

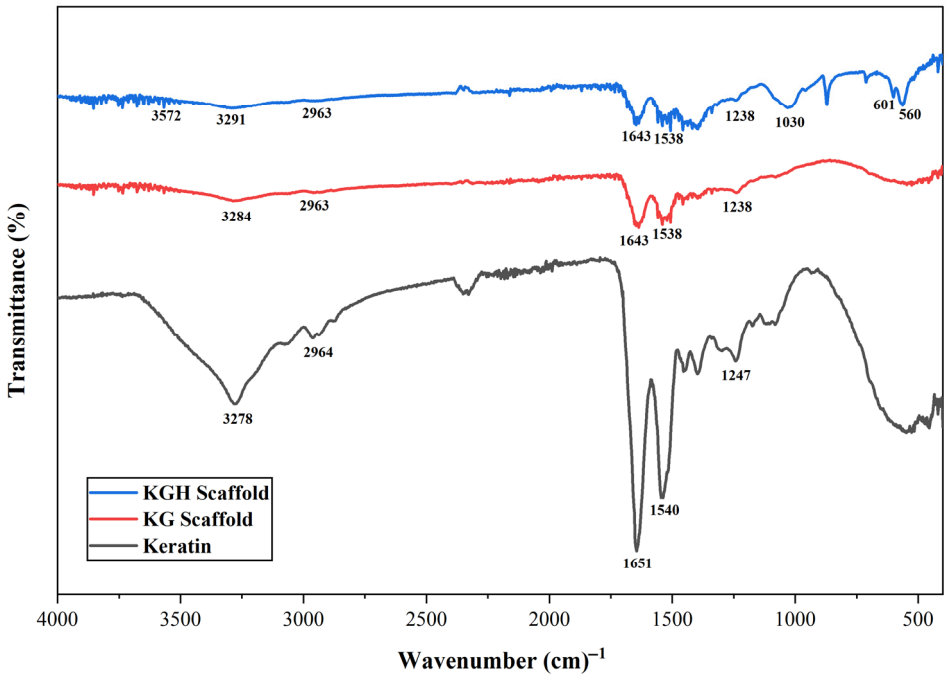


Figure 2. FTIR spectra of keratin from human nail clippings, the KG scaffold, and the KGH scaffold.

From the FTIR spectra of the KG scaffold displayed in Figure 2, all characteristic peaks associated with keratin are evident, with stretching vibrational absorption bands corresponding to N–H and C–N bonds observed at 3284 cm^{-1} and 2963 cm^{-1}, respectively. The absorption peak at 1643 cm^{-1} is attributed to the C=O stretching vibration of the Amide I band, which is particularly sensitive to the secondary structure of proteins. A prominent peak at 1538 cm^{-1} corresponds to N–H bending vibrations, indicative of the Amide II band. The broad peak at 1238 cm^{-1} and 2963 cm^{-1}, respectively. The absorption peak at 1643 cm^{-1} is attributed to the C=O stretching vibration of the Amide I band, which is particularly sensitive to the secondary structure of proteins. A prominent peak at 1538 cm^{-1} corresponds to N–H bending vibrations, indicative of the Amide II band. The broad peak at 1238 characteristic peaks associated with keratin are evident, with stretching vibrational absorption bands corresponding to N–H and C–N bonds observed at 3284 cm^{-1} and 2963 cm^{-1}, respectively. The absorption peak at 1643 cm^{-1} is attributed to the C=O stretching vibration of the Amide I band, which is particularly sensitive to the secondary structure of proteins. A prominent peak at 1538 cm^{-1} corresponds to N–H bending vibrations, indicative of the Amide II band. The broad peak at 1238 cm^{-1} corresponds to the N–H and C–N stretching vibrations of the Amide III band. Similarly to keratin, the FTIR spectra of gelatin also exhibit Amide I (C=O stretching and hydrogen bonding coupled with COO-), Amide II (N–H bending and stretching), and Amide III (in-plane vibrations of C–N and N–H bonds in bound amides) [59].

From the FTIR spectra of the KGH scaffold shown in Figure 2. The characteristic peaks observed at 3291 cm^{-1}, 2963 cm^{-1}, 1643 cm^{-1}, 1538 cm^{-1}, and 1238 cm^{-1} confirm the presence of N–H stretching, CH_3 stretching, and the Amide I, II, and III bands, respectively. In addition, absorption bands associated with HAp are evident. A distinct peak at 1030 cm^{-1} is attributed to phosphate groups, while a strong band at 3572 cm^{-1} corresponds to –OH stretching vibrations of water molecules. A peak at 560 cm^{-1} is assigned to the bending mode of the P-O-P group, further confirming the presence of phosphate groups in the HAp structure of the KGH scaffold [45,60].

3.3. XRD Analysis

The XRD patterns of keratin, the KG scaffold, and the KGH scaffold were shown in Figure 3. The XRD results indicate that the extracted keratin predominantly exists in a semicrystalline form. The diffraction peaks observed correspond to specific protein secondary structures. Meridional reflections around 0.51 nm (2θ between 15° and 31°) are characteristic of α-helix structures, while equatorial reflections at 0.98 nm (2θ = 9°) are attributed to β-sheet structures. Additionally, reflections at 0.465 nm (2θ between 16° and 31°) are associated with β-helix structure [61,62]. Diffraction patterns typical of α-helical configurations are represented by peaks appearing at 2θ = 8–9° [63,64]. In the current study, two strong peaks at 2θ = 10.67° and 21.92° are assigned to α-helix and β-sheet structures, respectively. These findings are consistent with those reported by Sharma et al. [56] for keratin extracted from feathers. Furthermore, a broad peak at 2θ = 13° is attributed to the amorphous region of the keratin. Notably, even after the regeneration process, partial crystallinity of the keratin is retained, as evidenced by the preserved diffraction characteristics [56].

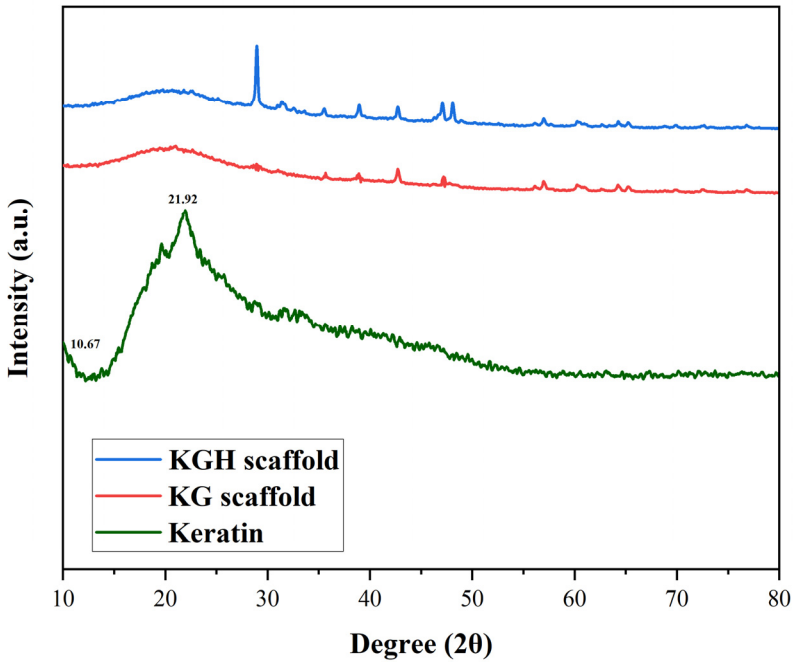


Figure 3. XRD pattern of keratin, the KG scaffold, and the KGH scaffold.

An increase in diffraction peak intensity is observed with higher HAp content, indicating enhanced crystallinity in the KGH scaffold (Figure 3). This increase is attributed to the incorporation of HAp, which contributes to the overall crystalline structure of the scaffold. The observed crystalline planes in the KGH scaffold further suggest that the freeze-drying method employed during scaffold fabrication preserved the crystalline phase of HAp, without inducing any phase transformation.

3.4. Microstructure and Pore Size Determination

SEM was used to investigate the morphology and microstructure of keratin, and the fabricated scaffolds at various magnifications, as shown in Figure 4. The extracted keratin protein, following lyophilization, was examined directly without further grinding into powder. As shown in Figure 4a,b, keratin exhibits a scaly, strand-like morphology, consistent with its fibrous protein structure.

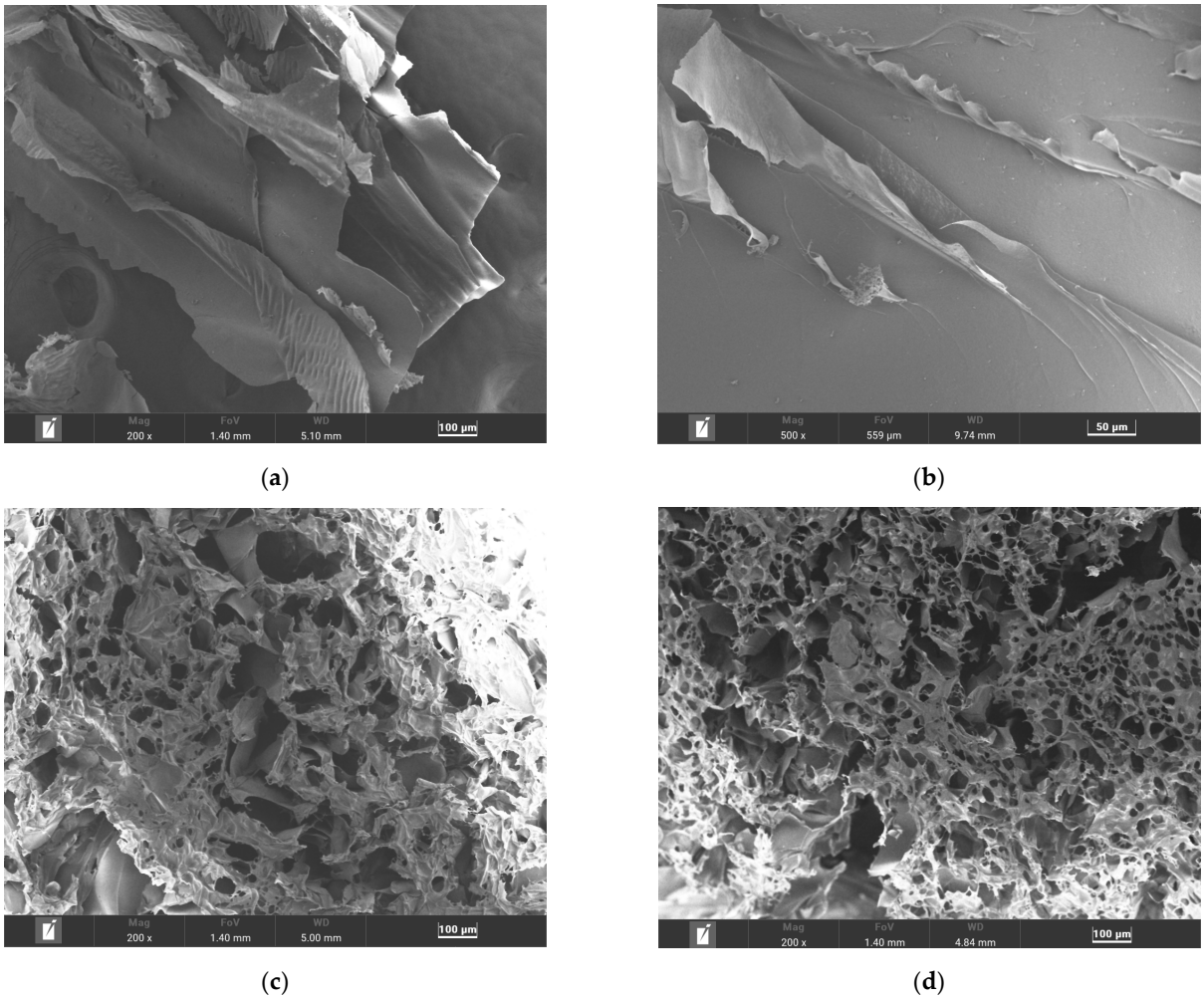


Figure 4. SEM images of (**a**,**b**) keratin, (**c**) the KG scaffold, and (**d**) the KGH scaffold.

Figure 4c,d show the microstructure of the KG and KGH scaffolds at 200× magnification. Both scaffolds exhibit a highly porous architecture with interconnected and heterogeneous pore size distribution. The average pore size was quantified using Feret diameter measurements via ImageJ (version 1.54g) software. The KG scaffold displays an average pore size of 109 µm, while the KGH scaffold has a slightly smaller average pore size of 100 µm. The reduction in pore size in the KGH scaffold is likely due to the incorporation of HAp, which may influence scaffold density and internal structure.

For effective tissue regeneration, scaffold pore architecture plays a crucial role. Generally, pore diameters of approximately 100 µm are considered optimal. Pores ranging from 50 to 100 µm support bone–cell attachment, while 40 to 100 µm promote vascular ingrowth, as reported by Mukasheva et al. [65]. In soft tissue applications such as skin and wound healing, smaller pores (1–20 µm) facilitate initial cell attachment, whereas 20–100 µm pores support nutrient diffusion. To balance mass transfer and cellular adhesion, many regenerative scaffolds are thus designed with average pore sizes close to 100 µm. Balaji et al. [66], for instance, developed freeze-dried keratin–gelatin hybrid scaffolds for wound healing, which revealed, via SEM, densely interconnected pores ranging between 20 and 100 µm, mostly in the tens of microns range. This pore size distribution falls within the ideal range for soft tissue regeneration and is comparable to the average pore sizes observed in the current study.

Scaffold fabrication methods, particularly freeze-drying, heavily influence pore structure. During freezing, ice crystals form an interconnected network that, upon sublimation,

leaves behind a sponge-like porous matrix [67,68]. Factors such as freezing rate, temperature, and polymer/filler composition (e.g., HAp) dictate final pore architecture [69]. Faster freezing and lower temperatures typically yield smaller, more frequent pores, while polymer-ceramic blends help preserve and define the pore network during sublimation [70,71].

While homogeneous porous scaffolds with uniform 100 μm pores offer predictable structural properties, heterogeneous (dual-scale) pore systems have been shown to significantly enhance cell colonization, nutrient transport, and angiogenic potential [72–75]. For instance, Sobral et al. reported that seeding efficiency of HOB cells was approximately 70% in a gradient–pore polycaprolactone (PCL) scaffold (100–700–100 μm), compared to only approximately 35% in a uniform 100 μm scaffold [72]. Similarly, Luca et al. demonstrated that mesenchymal stem cells (MSCs) in gradient scaffolds not only infiltrated deeper but also showed higher calcium deposition [73]. These results reflect the synergistic benefits of combining large pores, which allow for deep cell migration, with small pores, which offer higher surface areas for adhesion. Rasoulianboroujeni et al. demonstrated that dual-porosity collagen scaffolds—comprising small pores within the walls of larger ones—achieved both enhanced cell infiltration and more even cell distribution. This structural design optimally supports both early-stage cell attachment and long-term migration [74]. Functionally, heteroporous scaffolds also provide improved mass transport efficiency. Larger pores increase hydraulic permeability, enabling convective flow for waste removal, while smaller pores support diffusion-based nutrient delivery due to their high surface-to-volume ratios [74]. Computational models such as finite element, diffusion models, and computational fluid dynamics confirmed that scaffolds with higher effective diffusivity and permeability promote deeper cell survival and more robust bone formation, especially in thick constructs where diffusion limitations are common [74].

In line with this, heteroporous scaffolds, such as the KG and KGH scaffolds with average pore sizes of 109 μm and 100 μm, respectively, are expected to support better nutrient exchange, higher cell infiltration, and reduced hypoxic zones, compared to monolithic 100 μm scaffolds. This multi-scale porosity effectively replicates the hierarchical architecture of native bone. Furthermore, heteroporous designs are advantageous for angiogenesis. Larger pores (>100 μm) facilitate endothelial cell migration and capillary network formation, while smaller pores help retain pro-angiogenic factors like vascular endothelial growth factor (VEGF), concentrating signaling molecules within the matrix. Even in static in vitro systems, such designs enhance VEGF expression and matrix mineralization, both key to vascularization and tissue maturation [74]. These characteristics were shown to be stronger in graded or dual-porosity scaffolds than in homogeneous ones.

Collectively, the fabricated KG and KGH scaffolds—with their heterogeneous pore distribution—align with the literature findings that graded or heteroporous structures outperform uniform 100 μm scaffolds in promoting cell proliferation, angiogenic signaling, and nutrient transport. Studies consistently report 2–3× higher cell infiltration and vascularization efficiency in heteroporous systems, including PCL gradients, collagen sponges, and bioinspired composites [72,74]. This suggests that scaffolds like ours, which feature a range of pore sizes, more effectively mimic native extracellular matrices and provide a superior platform for soft tissue and bone regeneration. Although this study did not include cell-based evaluations, the architectural features of the fabricated scaffolds are consistent with previously reported designs known to support cell proliferation, migration, and nutrient diffusion. These findings provide a strong foundation for future investigations, particularly focusing on in vitro cell attachment and proliferation on the developed scaffolds.

3.5. Elemental Composition Analysis

EDX spectroscopy was employed to determine the elemental composition of the extracted keratin and the fabricated scaffolds. The amino acid composition of keratin predicts the presence of key elements such as carbon (C), nitrogen (N), oxygen (O), and sulfur (S). Carbon serves as the backbone of amino acid structures, while nitrogen is primarily found in peptide bonds. Oxygen appears in hydroxyl (-OH) and carboxyl (-COOH) groups and sulfur is characteristic of sulfur-containing amino acids such as cysteine and methionine.

The presence of sulfur is particularly important in keratin, a cysteine-rich protein, where disulfide bonds contribute significantly to the protein's mechanical stability. The EDX spectrum of lyophilized keratin (Figure 5) confirms the presence of the major expected elements: C, O, N, and S. In the KG scaffold (Figure 6), additional trace elements such as aluminum (Al), sodium (Na), and calcium (Ca) are also detected, likely introduced through the incorporation of gelatin or during the fabrication process. The composite nature of the KG scaffold is thus confirmed by the presence of both organic (C, N, O, and S) and inorganic (Na, Ca, and Al) components. The EDX spectrum of the KGH scaffold (Figure 7) shows the presence of C, O, N, Ca, Na, S, and phosphorus (P). The detection of Ca and P is consistent with the incorporation of HAp, which is composed primarily of calcium phosphate. The elemental profile confirms the successful integration of HAp into the scaffold matrix, as intended. These elemental analyses collectively confirm the expected composition of the raw materials and scaffolds, supporting the successful fabrication of the KG and KGH composites for potential biomedical applications. The elemental composition of keratin, the KG scaffold, and the KGH scaffold are summarized in Table 1.

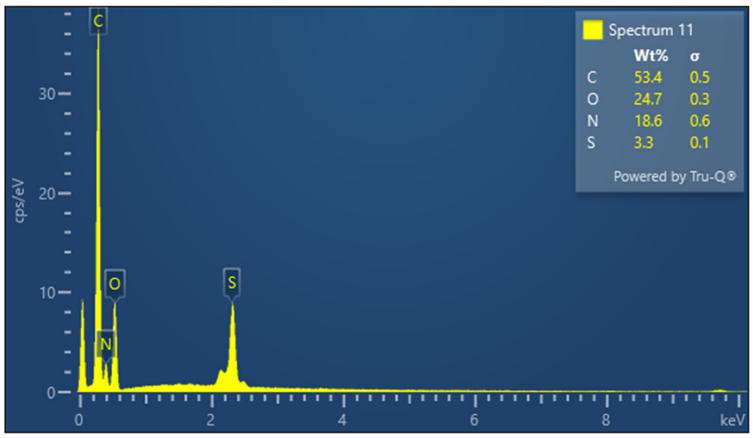


Figure 5. EDX spectra of keratin.

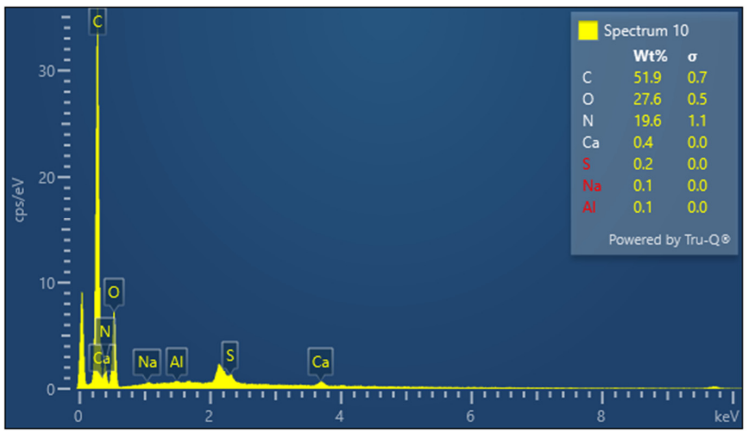


Figure 6. EDX spectra of the KG scaffold.

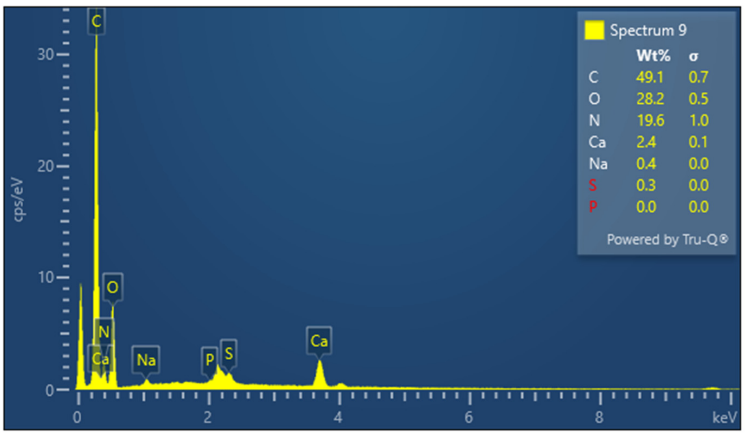


Figure 7. EDX spectra of the KGH scaffold.

Table 1. Elemental composition of keratin, the KG scaffold, and the KGH scaffold.

Sample	Element	Weight Percentage (%)	Standard Deviation (σ)
Keratin	C	53.4	0.5
	O	24.7	0.3
	N	18.6	0.6
	S	3.3	0.1
KG scaffold	C	51.9	0.7
	O	27.6	0.5
	N	19.6	1.1
	S	0.2	0.0
	Ca	0.4	0.0
	Na	0.1	0.0
	Al	0.1	0.0
KGH scaffold	C	49.1	0.7
	O	28.2	0.5
	N	19.6	1.0
	Ca	2.4	0.1
	Na	0.4	0.0
	S	0.3	0.0
	P	0.0	0.0

3.6. Water Uptake and Retention Capability

The water uptake and water retention capabilities of the KG and KGH scaffolds are shown in Figure 8. The results indicate that both scaffolds exhibit excellent water absorption, with the absorbed water content exceeding 100% of their original dry weight [50]. This suggests a strong affinity for water, which is characteristic of hydrophilic materials. However, the incorporation of HAp into the KGH scaffold led to a noticeable decrease in water uptake compared to the KG scaffold. This reduction is likely due to the partial occlusion of pores or increased scaffold density caused by the presence of HAp particles, which can reduce the scaffold's overall porosity and capacity to hold water.

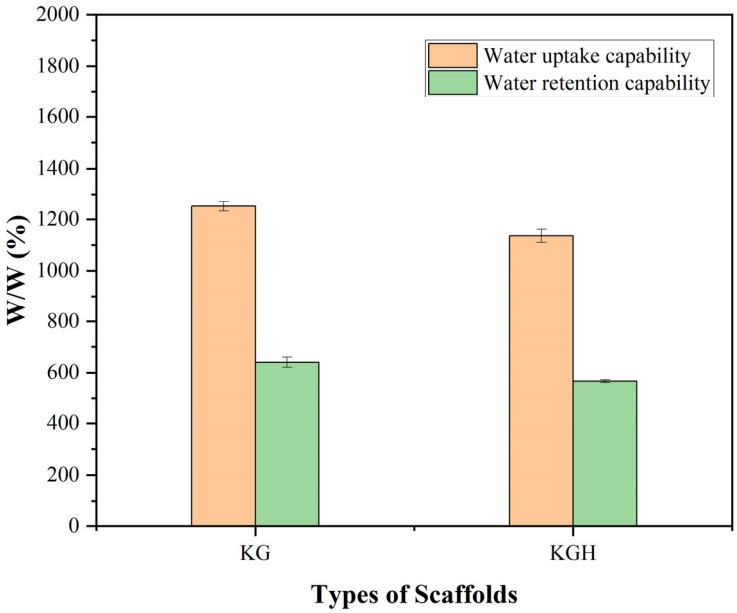


Figure 8. Water uptake and retention capability of the KG and KGH scaffolds after 24 h. Significant differences are observed between the KG and KGH scaffolds in both water uptake and retention ($p < 0.05$). Data are presented as mean ± SD ($n = 3$).

Protein-based scaffolds with high porosity typically exhibit substantial water absorption capacity. For example, Kakkar et al. developed a freeze-dried keratin–chitosan–gelatin scaffold that achieved an equilibrium water uptake exceeding 1700%, absorbing more than 17 times its dry weight [70]. Similarly, other protein-based materials such as collagen and gelatin have demonstrated swelling ratios of several hundred percent under comparable conditions. Even simpler keratin-based scaffolds without ceramic fillers (e.g., HAp) have shown notable hydrophilicity; for instance, a keratin/polyvinyl alcohol (PVA) scaffold reported by Mohamed et al. [76] exhibited approximately 84% water uptake after 24 h. However, the incorporation of HAp generally reduces water absorption. Studies have shown that pure gelatin/PVA scaffolds without HAp demonstrate significantly higher swelling, whereas the addition of HAp leads to a marked decrease in overall uptake [77]. Consistent with these findings, the present results indicate that KGH composite scaffold absorbs substantially less water than KG scaffold, which lacks ceramic filler and tend to exhibit much higher swelling ratios, often in the range of several hundred to over a thousand percent.

Despite the reduction in swelling with HAp incorporation, both KG and KGH scaffolds retained significant amounts of water over time, further confirming their hydrophilic character. This hydrophilicity is particularly advantageous for tissue engineering applications, as it facilitates nutrient diffusion, metabolic waste removal, cell proliferation and migration, and can enhance the localized retention and release of growth factors. Moreover, hydrophilic scaffolds better simulate the hydrated environment of the native extracellular matrix (ECM), thereby improving biological compatibility and promoting tissue integration in vivo [78].

3.7. Porosity

Scaffold porosity plays a critical role in regulating cell infiltration, nutrient transport, and overall tissue integration. The porosity of the fabricated scaffolds was evaluated using the liquid displacement method with ethanol as the displacement liquid. The average porosity values, based on three replicates, are shown in Figure 9. The KG scaffold exhibits a porosity of 84.59 ± 8.23%, while the KGH scaffold shows a slightly lower porosity of

78.26 ± 1.88%. As expected, the incorporation of HAp into the scaffold matrix results in a marginal reduction in porosity, attributed to partial pore filling or densification due to the presence of the HAp. Similar findings have been reported in other studies. For instance, Thein-Han and Misra [50] found that the addition of nano-HAp to chitosan–gelatin scaffolds reduced porosity from approximately 89% to 75% due to the physical occupation of pore space by the mineral phase. Likewise, Kim et al. [77] reported a notable reduction in porosity upon integrating HAp into gelatin/PVA scaffolds fabricated via 3D printing. The reduction was attributed to scaffold densification and a decrease in void volume resulting from increased solid content and mineral particle loading. Additionally, depending on the dispersion and aggregation of the ceramic phase within the polymer matrix, the incorporation of inorganic particles such as HAp can alter not only the pore size but also the interconnectivity of the pore network. While HAp enhances osteoconductivity and mechanical strength, excessive mineral loading may hinder mass transport within the scaffold, compromising its biological functionality [77,78].

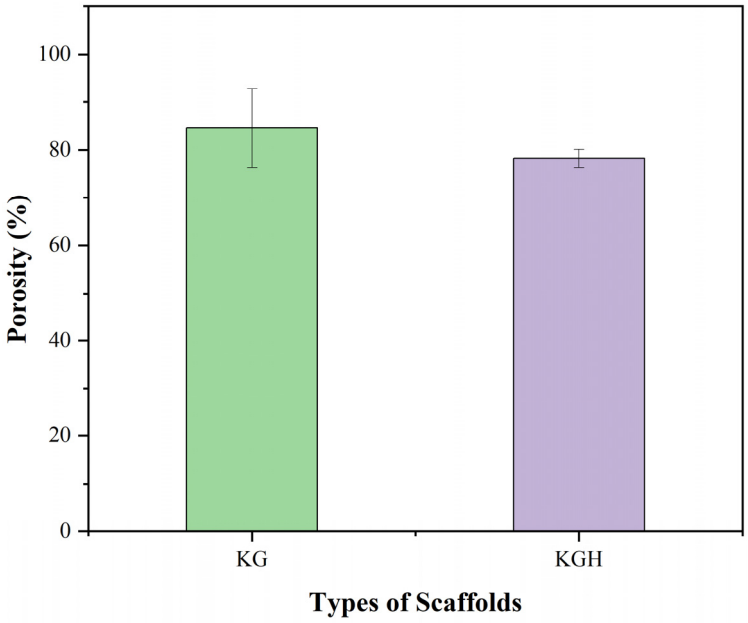


Figure 9. Porosity (%) of the KG and KGH scaffolds. The green colour represents the KG scaffold, while the purple colour represents the KGH scaffold. No significant difference is observed between the KG and KGH scaffolds ($p > 0.05$). Data are presented as mean ± SD ($n = 3$).

Therefore, it is essential to strike a balance between bioactivity and porosity to optimize scaffold performance. Although the inclusion of HAp decreases the pore volume of the KGH scaffold, the difference is not statistically significant. These results align with previous studies reporting that moderate HAp inclusion can be accomplished without substantial compromise to scaffold porosity. Specifically, composite scaffolds fabricated by varying HAp concentrations with a fixed amount of gelatin solution demonstrated only slight reductions in porosity, reinforcing the conclusion that moderate HAp addition maintains structural integrity and pore interconnectivity [79]. Importantly, both KG and KGH scaffolds exhibit porosity levels well above 30%, the minimum threshold generally considered sufficient for effective cell proliferation, nutrient diffusion, and metabolic waste removal [80]. High porosity is also crucial for promoting tissue integration and ensuring that by-products of scaffold degradation can be eliminated without hindrance. The porosity values obtained in this study suggest that both scaffolds meet essential criteria for tissue engineering applications, supporting cell adhesion, migration, and differentiation within the scaffold matrix.

3.8. Tensile Strength

The mechanical performance of the KG and KGH scaffolds was assessed through tensile testing, with key parameter Young's modulus, calculated by the stress–strain curve. Young's modulus (Figure 10) shows a statistically significant difference ($p < 0.05$), indicating a notable variation in the elastic stiffness of the scaffolds. The average Young's modulus is recorded as 1.66 ± 0.29 MPa for the KG scaffold and 0.87 ± 0.19 MPa for the KGH scaffold. The observed decrease in stiffness for the KGH scaffold is attributed to weak interfacial bonding between the keratin–gelatin matrix and the HAp particles, which can create stress concentration points and facilitate premature mechanical failure under tensile loading [81]. This phenomenon reflects a common challenge in composite scaffold fabrication, where balancing bioactivity with mechanical integrity requires careful material design. Similar mechanical behavior was reported in a recent study, where composite scaffolds containing 10% nano-HAp and β-tricalcium phosphate (β-TCP) showed comparable Young's modulus values around 0.947 MPa [49]. Despite the reduction in Young's modulus upon HAp incorporation, both scaffolds exhibit mechanical properties that are suitable for applications in non-load-bearing bone repair. Specifically, the stiffness and flexibility of the KG and KGH scaffolds fall within the optimal range for treating orofacial bone defects caused by trauma, cysts, inflammation, or tumors, areas that demand biocompatible scaffolds with sufficient mechanical integrity but not necessarily a high-load bearing capacity [49].

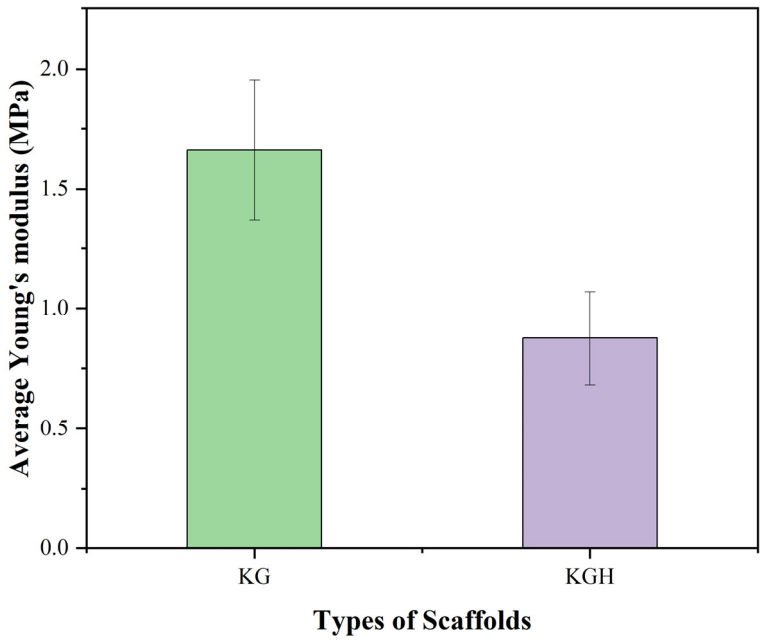


Figure 10. Young's modulus of the KG and KGH scaffolds. The green colour represents the KG scaffold, while the purple colour represents the KGH scaffold. There is a significant difference in Young's modulus between the KG and KGH scaffolds ($p < 0.05$). The values are represented in mean ± SD ($n = 3$).

The stiffness of porous scaffolds, commonly measured as Young's modulus, is inversely correlated with porosity. As porosity increases, the effective elastic modulus decreases significantly due to the reduction in solid load-bearing material within the structure [82]. The KG scaffolds, typically fabricated via freeze-drying, possess a highly interconnected porous network with pore diameters ranging from 20 to 100 µm and porosities often between 70% and 90%. While such high porosity is beneficial for cell infiltration and nutrient diffusion, it inherently compromises mechanical stiffness. For example, Balaji et al. developed freeze-dried keratin–gelatin sponges with pore sizes in the range of 20–100 µm

and reported that, although the scaffolds demonstrated biocompatibility and structural integrity, their tensile strength was limited to approximately 1–2 MPa. These scaffolds also exhibited significant extensibility under applied stress, indicating a low initial stiffness in the absence of additional crosslinking strategies. This mechanical behavior reflects a low Young's modulus, which is consistent with the high void fraction of the material [64].

Previous experimental studies have shown that scaffold stiffness can be effectively modulated by altering the composition to control porosity. For instance, in gelatin–starch blends, increasing the gelatin content—a highly hydrophilic component—promoted pore formation during lyophilization, resulting in porosity levels as high as 90%. This, in turn, led to a notable reduction in mechanical strength. Conversely, reducing the gelatin fraction while increasing the proportion of the less porous filler (starch) yielded denser scaffolds with enhanced mechanical strength. These findings support the general observation that porosity and mechanical strength are inversely correlated: scaffolds with a higher solid polymer content (i.e., lower porosity) tend to exhibit greater stiffness and strength. A similar trend was observed in gelatin-only hydrogels, where increasing the gelatin concentration—thereby raising the polymer density and reducing free water—resulted in higher Young's modulus due to improved load-bearing capacity. Collectively, these insights highlight the importance of porosity control—through composition or processing methods—as a key strategy for tuning the mechanical properties of the KG scaffolds. Variants with higher porosity tend to be softer and more compliant, while those with lower porosity or increased cross-linking (which effectively raises the solid phase density) exhibit greater mechanical stability and higher elastic moduli [83,84].

The addition of HAp—a ceramic phase—to the KG scaffolds significantly affects both porosity and stiffness. Incorporating HAp typically results in a moderate reduction in overall porosity, as the ceramic particles occupy void spaces, while concurrently producing a notable increase in stiffness by reinforcing the polymer matrix and enhancing its load-bearing capacity [79]. Contrary to trends commonly reported in the literature, our findings revealed that the incorporation of HAp into the KG scaffolds led to a reduction in both porosity and tensile-derived Young's modulus. While HAp is traditionally used as a reinforcement agent due to its inherent stiffness and bone-mimetic properties, the unexpected decrease in scaffold stiffness suggests inefficient stress transfer between the inorganic filler and the organic matrix. This mechanical behavior may be attributed to disrupted structural homogeneity following HAp incorporation, potentially resulting from poor interfacial adhesion or agglomeration of HAp particles within the matrix. Such microstructural inconsistencies can act as stress concentrators, ultimately compromising the scaffold's mechanical integrity and reducing its effective modulus [85].

Furthermore, the densification effect associated with reduced porosity may have compromised the scaffold's ability to deform elastically, rendering it less compliant and more brittle under tensile loading. These findings suggest that reducing porosity alone does not necessarily lead to improved mechanical strength, particularly when the filler–matrix interaction is suboptimal. Instead, the mechanical performance of composite scaffolds is highly dependent on the uniform dispersion of the inorganic phase and the quality of interfacial bonding between the ceramic filler and the polymeric matrix. This underscores the importance of carefully optimizing HAp distribution and surface chemistry within KG systems to achieve structurally robust and mechanically reliable scaffolds.

3.9. Biocompatability Analysis

Figure 11 shows a statistically significant difference in cell viability between the three groups (2D control, KG scaffold, and KGH scaffold) over the five-day culture period ($p < 0.05$). Initially (Day 0), an equal number of cells (3.4×10^4) were seeded in all three sys-

tems. Over time, all groups exhibited a marked increase in cell numbers, indicating healthy cell proliferation. On Day 1, the KG scaffold supported approximately 6.97×10^5 cells; the KGH scaffold supported 1.34×10^6 cells; and the 2D control had about 7.72×10^5 cells. By Day 5, cell counts had approximately tripled in each group: the KG scaffold supported 2.22×10^6 cells, the KGH scaffold 3.98×10^6 cells, and the control 2.19×10^6 cells, all with >90% cell viability. Notably, the HAp-containing KGH scaffold consistently maintained the highest number of viable cells at each time point.

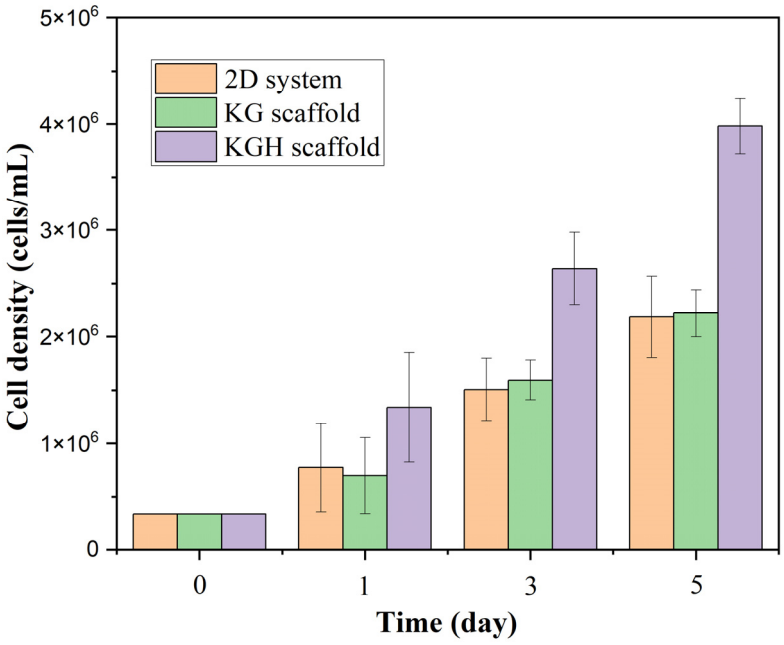


Figure 11. Cell viability of the control (2D), KG, and KGH scaffolds from Day 1 to Day 5. Data are presented as mean ± SD (with n = 3 biological replicates per group).

All groups showed strong overall proliferation under standard culture conditions. The 2D control system exhibited steady growth, while the KG scaffold maintained comparable cell viability, suggesting no inhibitory effect on cell proliferation. Importantly, by Day 5, the viable cell count on the KGH scaffold was approximately 1.8–1.9 times higher than that of the KG scaffold and the control. These findings imply that although both scaffolds were biocompatible, the incorporation of HAp significantly enhanced cell proliferation.

This observation aligns with the well-established roles of keratin and gelatin in mimicking the ECM environment. Gelatin, a derivative of collagen, contains Arg–Gly–Asp (RGD) motifs known to interact with cell-surface integrins, thereby promoting cell adhesion and spreading [86]. Similarly, keratin contains natural cell-binding sequences and bioactive domains, often comparable to those found in collagen peptides, which further support cellular attachment and viability. Consistent with these findings, Kakkar et al. reported strong fibroblast viability on keratin–chitosan–gelatin scaffolds, highlighting the biocompatibility of keratin-based composites. In the present study, the near-equivalent cell viability between the 2D control and the KG scaffold suggests that the cells readily adhered to and proliferated on the scaffold, likely due to the synergistic presence of RGD-like motifs in gelatin and the cell-interactive domains of keratin [70].

The most significant finding of this study is the enhanced cell proliferation observed on the HAp-containing scaffold (KGH). At every time point, the number of viable cells on the KGH scaffold was markedly higher than that on the KG scaffold or the 2D control. By Day 5, the KGH scaffold supported approximately 4.0×10^6 viable cells, while both the KG scaffold and control supported around 2.2×10^6 cells. This represents an increase of approximately

80–90%, indicating that HAp exerts a strong stimulatory effect on cell proliferation. HAp is widely recognized as a highly biocompatible and osteoconductive biomaterial that closely mimics the mineral composition of native bone and teeth. Its incorporation into scaffolds likely creates a more favorable microenvironment for osteoblasts by providing both physical and chemical cues. Physically, HAp particles increase surface roughness and offer more adhesion sites, enhancing cell attachment. Chemically, they can release calcium and phosphate ions into the culture medium, which are known to trigger signaling pathways involved in cell division, survival, and osteogenic differentiation. These findings are consistent with previous reports, including those by Liu et al., who demonstrated that HAp not only supports bone formation but also exhibits excellent biocompatibility and osteoinductive properties [87].

Similarly, recent studies on HAp/gelatin scaffolds have demonstrated that HAp-based composites are non-toxic and support high levels of cell viability, with over 70% survival and a significant increase in cell numbers over several days. Our findings align well with these earlier reports: the HAp-enriched scaffold (KGH) promoted substantial cell proliferation and exhibited no cytotoxic effects, enabling cells to not only survive but thrive. In particular, one study reported that HAp/PCL/gelatin nanofiber scaffolds enhanced cell adhesion and proliferation, leading to progressive increases in cell viability from Day 1 to Day 5—an outcome attributed to the osteoinductive properties of HAp. Although the material composition in our study differs, the observed trend is consistent: the incorporation of HAp significantly boosts cell growth over time by providing bioactive cues that support cellular activities critical for bone tissue regeneration [88].

The significance of incorporating HAp becomes evident when comparing the KG and KGH scaffolds. While the KG matrix alone maintains cell viability, it supports only baseline levels of proliferation in the absence of HAp. The addition of HAp in the KGH scaffold markedly enhances proliferation, indicating a synergistic effect between the scaffold components. In this system, HAp provides osteoinductive biochemical cues, while keratin and gelatin contribute a bioactive interface, offering structural support and adhesion-promoting ligands. It is well documented that calcium ions released from HAp can upregulate osteogenic gene expression and activate signaling pathways associated with osteoblast differentiation and proliferation. This ionic stimulation likely accelerates cell division. Additionally, due to its high surface energy, HAp has a strong capacity to adsorb serum proteins from the culture medium, further enhancing initial cell attachment and spreading [87,88].

4. Conclusions

In this study, keratin was successfully synthesized and incorporated into the fabrication of the KG and KGH scaffolds, which were subsequently characterized to evaluate their potential for tissue engineering applications. The KG scaffold was formulated using a blend of natural biopolymers, keratin and gelatin, known for their biocompatibility and biodegradability. To enhance bioactivity and osteoconductive properties, HAp was added to the composite, resulting in the KGH scaffold variant.

FTIR confirmed the successful incorporation of individual scaffold components by identifying characteristic functional groups. In the KGH scaffold, distinct phosphate and hydroxyl peaks verified the presence of HAp, indicating that its addition did not disrupt the structural integrity of the biopolymer matrix. Further confirmation was provided by XRD analysis, which revealed the presence of crystalline HAp in the KGH scaffold, while the KG scaffold remained predominantly amorphous. The formation of a crystalline phase in the KGH scaffold is critical for mimicking the mineral composition of natural bone and supporting osteogenic differentiation.

SEM analysis revealed the porous, scaly, and strand-like morphology characteristic of keratin. Both KG and KGH scaffolds exhibited a highly porous, heteroporous, and interconnected architecture, which is essential for facilitating cell infiltration, nutrient diffusion, and vascularization. The average pore sizes in both scaffolds fell within the optimal range for bone tissue engineering, with the KGH scaffold displaying slightly reduced porosity due to HAp particle deposition, which partially filled the void spaces.

Water uptake and retention studies demonstrated that both KG and KGH scaffolds effectively balanced structural stability with hydration capacity. While the KG scaffold exhibited higher swelling, the KGH scaffold showed significantly reduced water absorption, likely due to HAp particle incorporation, which partially occupied pore spaces. Despite lower swelling, KGH maintained enhanced mechanical integrity, a desirable attribute for in vivo applications. These findings were further supported by porosity measurements, which aligned with SEM observations, confirming that the KG scaffold was more porous than its KGH counterpart.

The Young's modulus of both KG and KGH scaffolds reflects their unique elastic stiffness, which can influence cell migration and differentiation, despite their similar load-bearing and elongation capacities. Interestingly, the KGH scaffold exhibited lower Young's modulus compared to the KG scaffold, which raises concerns regarding its mechanical performance. This reduction may be attributed to weak interfacial bonding between the HAp and the keratin–gelatin matrix, potentially leading to poor stress transfer and mechanical discontinuity. Therefore, further investigation into interfacial interactions and HAp dispersion within the composite is warranted. Nonetheless, the measured modulus for the KGH scaffold remains comparable to values reported in recent studies, supporting its potential applicability in repairing bone defects, particularly in non-load-bearing regions where lower stiffness is acceptable.

Beyond being non-toxic, the biocompatibility assessment demonstrates that the HAp-enriched scaffold actively promotes cell proliferation. This enhancement is likely driven by a combination of physical cues—such as increased surface roughness—and biochemical effects, including calcium and phosphate ion release and osteogenic signaling. The elevated cell viability observed on the KGH scaffold underscores its strong potential for bone tissue engineering and other regenerative applications where high cellularity is critical. While future studies could explore specific molecular mechanisms, such as signaling pathways or the expression of osteogenic differentiation markers, the current results provide clear evidence of the superior biocompatibility and proliferation-supporting properties of HAp-containing scaffolds. These findings position the KGH composite as a promising candidate for further development in bone regenerative therapies.

For future studies, in vitro biocompatibility assays (WST-1 assays or MTT assays) will be conducted to validate the clinical relevance of these scaffolds. These experiments are expected to provide detailed insights into the cellular response and osteogenic potential of both scaffold types. Additionally, in vitro biodegradation tests under physiological conditions will be performed to assess degradation kinetics and the long-term stability of the materials. Understanding the degradation profile will be essential to ensure scaffold resorption aligns with tissue regeneration rates, which is particularly important for bone repair applications. These planned investigations will support the optimization of scaffold design and facilitate progression toward clinical and translational implementation.

The KGH scaffold's fixed keratin-to-HAp ratio was used in this investigation in accordance with previous literature recommendations and the success of the initial formulation. The lack of systematic ratio screening, which could have affected scaffold performance attributes like mechanical strength, porosity, and cell responsiveness, is acknowledged. Using statistical modeling techniques and thorough screening, future research will try

to maximize the keratin–HAp mix ratio in order to increase bone tissue regeneration functionality. The importance of specific surface area analysis, particularly through the Brunauer–Emmett–Teller (BET) method, is acknowledged. However, due to current limitations in equipment availability, BET analysis could not be conducted in this study. This is recognized as a limitation and will be considered in future work. The dosage-dependent effects of HAp on porosity and mechanical strength were not evaluated, despite the fact that the current investigation used a fixed HAp content of 3% (*w*/*v*). In order to determine the best formulation for bone scaffold applications, future research will methodically assess various doses. The trypan blue exclusion experiment was used to evaluate cell viability; however, it does not offer a thorough understanding of cellular distribution or functional activity. Future research will use fluorescent live/dead staining to visualize spatial viability and cell-scaffold interaction more clearly. Moreover, molecular methods will be used to examine the expression of osteogenic differentiation markers including alkaline phosphatase (ALP) and osteocalcin (OCN) in order to validate the scaffold's osteoinductive qualities.

Remarkably, the KGH scaffold had lower Young's modulus than the KG scaffold, which challenges the common perception that HAp increases mechanical stiffness. Due to either insufficient chemical interaction or inhomogeneous HAp dispersion, this result could be explained by inefficient interfacial bonding between keratin and HAp. A conclusive conclusion is limited by the lack of high-resolution or elemental mapping data, even though SEM pictures did not show significant agglomerates or interfacial fissures. In order to better investigate the microstructural integrity and filler distribution inside the composite matrix, future research combining SEM–EDX analysis and cross-sectional imaging is planned.

Author Contributions: Conceptualization, H.S.; methodology, M.K., J.N.C. and W.R.L.; software, M.K., J.N.C. and W.R.L.; validation, M.K. and H.S.; formal analysis, M.K., J.N.C. and W.R.L.; investigation, M.K., J.N.C. and W.R.L.; resources, M.K., J.N.C., W.R.L. and N.J.; data curation, M.K., J.N.C. and W.R.L.; writing—original draft preparation, M.K.; writing—review and editing, M.K., N.J., N.S.S. and H.S.; supervision, N.S.S. and H.S.; project administration, H.S.; funding acquisition, H.S. All authors have read and agreed to the published version of the manuscript.

Funding: The APC was funded by the Universiti Brunei Darussalam Research Grant No. UBD/RSCH/1.3/FICBF(b)/2020/005.

Informed Consent Statement: Informed consent was obtained from all subjects involved in the study.

Data Availability Statement: The data presented in this study are openly available in the article.

Conflicts of Interest: The authors declare no conflicts of interest.

References

1. Baneshi, N.; Moghadas, B.K.; Adetunla, A.; Yusof, M.Y.P.M.; Dehghani, M.; Khandan, A.; Saber-Samandari, S.; Toghraie, D. Investigation the mechanical properties of a novel multicomponent scaffold coated with a new bio-nanocomposite for bone tissue engineering: Fabrication, simulation and characterization. *J. Mater. Res. Technol.* **2021**, *15*, 5526–5539. [CrossRef]
2. Li, X.; Wang, Y.; Wang, Z.; Qi, Y.; Li, L.; Zhang, P.; Chen, X.; Huang, Y. Composite PLA/PEG/nHA/Dexamethasone Scaffold Prepared by 3D Printing for Bone Regeneration. *Macromol. Biosci.* **2018**, *18*, e1800068. [CrossRef] [PubMed]
3. Krishani, M.; Shin, W.Y.; Suhaimi, H.; Sambudi, N.S. Development of Scaffolds from Bio-Based Natural Materials for Tissue Regeneration Applications: A Review. *Gels* **2023**, *9*, 100. [CrossRef] [PubMed]
4. Mistry, A.S.; Mikos, A.G. Tissue engineering strategies for bone regeneration. In *Regenerative Medicine II. Advances in Biochemical Engineering*; Yannas, I.V., Ed.; Springer: Berlin/Heidelberg, Germany, 2005; Volume 94. [CrossRef]
5. Alizadeh-Osgouei, M.; Li, Y.; Wen, C. A comprehensive review of biodegradable synthetic polymer-ceramic composites and their manufacture for biomedical applications. *Bioact. Mater.* **2019**, *4*, 22–36. [CrossRef] [PubMed]
6. Asadian, M.; Chan, K.V.; Norouzi, M.; Grande, S.; Cools, P.; Morent, R.; De Geyter, N. Fabrication and plasma modification of nanofibrous tissue engineering scaffolds. *Nanomaterials* **2020**, *10*, 119. [CrossRef] [PubMed]

7. Sabir, M.I.; Xu, X.; Li, L. A review on biodegradable polymeric materials for bone tissue engineering applications. *J. Mater. Sci.* **2009**, *44*, 5713–5724. [CrossRef]
8. Mariani, E.; Lisignoli, G.; Borzì, R.M.; Pulsatelli, L. Biomaterials: Foreign bodies or tuners for the immune response? *Int. J. Mol. Sci.* **2019**, *20*, 636. [CrossRef] [PubMed]
9. Ranjit, E.; Hamlet, S.; George, R.; Sharma, A.; Love, R.M. Biofunctional approaches of wool-based keratin for tissue engineering. *J. Sci. Adv. Mater. Devices* **2022**, *7*, 100398. [CrossRef]
10. McLellan, J.; Thornhill, S.G.; Shelton, S.; Kumar, M. Keratin-based biofilms, hydrogels, and biofibers. In *Keratin as a Protein Biopolymer: Extraction from Waste Biomass and Applications*; Sharma, S., Kumar, A., Eds.; Springer: Cham, Switzerland, 2019; pp. 187–200.
11. Cardamone, J.M.; Nuñez, A.; Garcia, R.A.; Aldema-Ramos, M.; Van Vliet, K.J. Characterizing wool keratin. *Adv. Mater. Sci. Eng.* **2009**, *2009*, 1–6. [CrossRef]
12. Fraser, R.D.B.; MacRae, T.P.; Rogers, G.E. *Keratins: Their Composition, Structure, and Biosynthesis*; Thomas: Springfield, IL, USA, 1972.
13. Schweizer, J.; Bowden, P.E.; Coulombe, P.A.; Langbein, L.; Lane, E.B.; Magin, T.M.; Maltais, L.; Omary, M.B.; Parry, D.A.; Rogers, M.A.; et al. New consensus nomenclature for mammalian keratins. *J. Cell Biol.* **2006**, *174*, 169–174. [CrossRef] [PubMed]
14. Li, Y.; Wang, Y.; Ye, J.; Yuan, J.; Xiao, Y. Fabrication of poly (ε-caprolactone)/keratin nanofibrous mats as a potential scaffold for vascular tissue engineering. *Mater. Sci. Eng. C* **2016**, *68*, 177–183. [CrossRef] [PubMed]
15. Navarro, J.; Swayambunathan, J.; Lerman, M.; Santoro, M.; Fisher, J.P. Development of keratin-based membranes for potential use in skin repair. *Acta Biomater.* **2019**, *83*, 177–188. [CrossRef] [PubMed]
16. Potter, N.A.; Van Dyke, M. Effects of differing purification methods on properties of keratose biomaterials. *ACS Biomater. Sci. Eng.* **2018**, *4*, 1316–1323. [CrossRef] [PubMed]
17. Spearman, R.I.C. On the nature of the horny scales of the pangolin. *Zool. J. Linn. Soc.* **1967**, *46*, 267–273. [CrossRef]
18. Fraser, R.D.B.; Parry, D.A.D. The structural basis of the filament-matrix texture in the avian/reptilian group of hard β-keratins. *J. Struct. Biol.* **2011**, *173*, 391–405. [CrossRef] [PubMed]
19. Squire, J.; Vibert, P.J.; Elliott, A. *Fibrous Protein Structure: A Volume Dedicated to Dr Arthur Elliott*; Academic Press: London, UK; San Diego, CA, USA, 1987.
20. Park, M.; Kim, B.-S.; Shin, H.K.; Park, S.-J.; Kim, H.-Y. Preparation and characterization of keratin-based biocomposite hydrogels prepared by electron beam irradiation. *Mater. Sci. Eng. C* **2013**, *33*, 5051–5057. [CrossRef] [PubMed]
21. Poole, A.J.; Lyons, R.E.; Church, J.S. Dissolving feather keratin using sodium sulfide for bio-polymer applications. *J. Polym. Environ.* **2011**, *19*, 995–1004. [CrossRef]
22. Korniłłowicz-Kowalska, T.; Bohacz, J. Biodegradation of keratin waste: Theory and practical aspects. *Waste Manag.* **2011**, *31*, 1689–1701. [CrossRef] [PubMed]
23. Tonin, C.; Aluigi, A.; Varesano, A.; Vineis, C. Keratin-based nanofibers. In *Nanofibers*; Kumar, A., Ed.; InTech: Croatia, Yugoslavia, 2010; pp. 139–158.
24. Sarrami, P.; Karbasi, S.; Farahbakhsh, Z.; Bigham, A.; Rafienia, M. Fabrication and characterization of novel polyhydroxybutyrate-keratin/nanohydroxyapatite electrospun fibers for bone tissue engineering applications. *Int. J. Biol. Macromol.* **2022**, *220*, 1368–1389. [CrossRef] [PubMed]
25. Siyum, S. Human Hair Keratin Protein, Hair Fibers and Hydroxyapatite Composite Scaffold for Bone Tissue Regeneration. Master's Thesis, Cleveland State University, Cleveland, OH, USA, 2014.
26. Kitahara, T.; Ogawa, H. The extraction and characterization of human nail keratin. *J. Dermatol. Sci.* **1991**, *2*, 402–406. [CrossRef] [PubMed]
27. Bean, W.B. Nail growth. Thirty-five years of observation. *Arch. Intern. Med.* **1980**, *140*, 73–76. [CrossRef] [PubMed]
28. Chilakamarry, C.R.; Mahmood, S.; Saffe, S.N.B.M.; Bin Arifin, M.A.; Gupta, A.; Sikkandar, M.Y.; Begum, S.S.; Narasaiah, B. Extraction and application of keratin from natural resources: A review. *3 Biotech* **2021**, *11*, 1–12. [CrossRef] [PubMed]
29. Baswan, S.; Kasting, G.B.; Li, S.K.; Wickett, R.; Adams, B.; Eurich, S.; Schamper, R. Understanding the formidable nail barrier: A review of the nail microstructure, composition and diseases. *Mycoses* **2017**, *60*, 284–295. [CrossRef] [PubMed]
30. Feroz, S.; Muhammad, N.; Ratnayake, J.; Dias, G. Keratin—Based materials for biomedical applications. *Bioact. Mater.* **2020**, *5*, 496–509. [CrossRef] [PubMed]
31. Skopinska-Wisniewska, J.; Tuszynska, M.; Olewnik-Kruszkowska, E. Comparative study of gelatin hydrogels modified by various cross-linking agents. *Materials* **2021**, *14*, 396. [CrossRef] [PubMed]
32. Natu, M.V.; Sardinha, J.P.; Correia, I.J.; Gil, M.H. Controlled release gelatin hydrogels and lyophilisates with potential application as ocular inserts. *Biomed. Mater.* **2007**, *2*, 241–249. [CrossRef] [PubMed]
33. Echave, M.C.; Hernáez-Moya, R.; Iturriaga, L.; Pedraz, J.L.; Lakshminarayanan, R.; Dolatshahi-Pirouz, A.; Taebnia, N.; Orive, G. Recent advances in gelatin-based therapeutics. *Expert Opin. Biol. Ther.* **2019**, *19*, 773–779. [CrossRef] [PubMed]

34. Huang, S.; Fu, X. Naturally derived materials-based cell and drug delivery systems in skin regeneration. *J. Control. Release* **2010**, *142*, 149–159. [CrossRef] [PubMed]
35. Jaipan, P.; Nguyen, A.; Narayan, R.J. Gelatin-based hydrogels for biomedical applications. *MRS Commun.* **2017**, *7*, 416–426. [CrossRef]
36. Young, S.; Wong, M.; Tabata, Y.; Mikos, A.G. Gelatin as a delivery vehicle for the controlled release of bioactive molecules. *J. Control. Release* **2005**, *109*, 256–274. [CrossRef] [PubMed]
37. Bello, A.B.; Kim, D.; Kim, D.; Park, H.; Lee, S.-H. Engineering and Functionalization of Gelatin Biomaterials: From Cell Culture to Medical Applications. *Tissue Eng. Part B Rev.* **2020**, *26*, 164–180. [CrossRef] [PubMed]
38. Bigi, A.; Cojazzi, G.; Panzavolta, S.; Roveri, N.; Rubini, K. Stabilization of gelatin films by crosslinking with genipin. *Biomaterials* **2002**, *23*, 4827–4832. [CrossRef] [PubMed]
39. Tonda-Turo, C.; Gentile, P.; Saracino, S.; Chiono, V.; Nandagiri, V.K.; Muzio, G.; Canuto, R.A.; Ciardelli, G. Comparative analysis of gelatin scaffolds crosslinked by genipin and silane coupling agent. *Int. J. Biol. Macromol.* **2011**, *49*, 700–706. [CrossRef] [PubMed]
40. Ranganathan, S.; Balagangadharan, K.; Selvamurugan, N. Chitosan and gelatin-based electrospun fibers for bone tissue engineering. *Int. J. Biol. Macromol.* **2019**, *133*, 354–364. [CrossRef] [PubMed]
41. Hossan, M.J.; Gafur, M.A.; Kadir, M.R.; Karim, M.M. Preparation and Characterization of Gelatin-Hydroxyapatite Composite for Bone Tissue Engineering. *Int. J. Eng. Technol. Sci.* **2014**, *14*, 24.
42. Rad, M.M.; Saber-Samandari, S.; Sadighi, M.; Tayebi, L.; Aghdam, M.M.; Khandan, A. Macro-and micromechanical modelling of HA-Elastin scaffold fabricated using freeze drying technique Nanocomposite Scaffold Mechanical property Wollastonite-HA ceramic Micromechanical model. *J. Nanoanal.* **2021**, *8*, 15.
43. Krishani, M.; Suhaimi, H.; Sambudi, N.S. *A Review of Hydroxyapatite: Sustainable Product Development in Terms of Waste Valorization*; Nova Science Publishers: New York, NY, USA, 2023.
44. Tu, H.; Yu, W.; Duan, L. Structural studies and macro-performances of hydroxyapatite-reinforced keratin thin films for biological applications. *J. Mater. Sci.* **2016**, *51*, 9573–9588. [CrossRef]
45. Murugiah, K.; Zakaria, M.I.; Suhaimi, H.; Caesarendra, W.; Sambudi, N.S. Synthesis and Characterisation of Hydroxyapatite (HAp) from Asiatic Hard Clam (Meretrix meretrix) and Blood Cockle Clam (Anadara granosa) Using Wet Precipitation Process. In Proceedings of the 2021 IEEE National Biomedical Engineering Conference (NBEC), Kuala Lumpur, Malaysia, 9–10 November 2021; pp. 1–6. [CrossRef]
46. Fereshteh, Z. Freeze-drying technologies for 3D scaffold engineering. In *Functional 3D Tissue Engineering Scaffolds: Materials, Technologies, and Applications*; Elsevier: Amsterdam, The Netherlands, 2018; pp. 151–174. [CrossRef]
47. Paramasivam, S.; Perumal, S.S. Methanolic extract of O.umbellata L. exhibits anti-osteoporotic effect via promoting osteoblast proliferation in MG-63 cells and inhibiting osteoclastogenesis in RANKL-stimulated RAW 264.7 cells. *J. Ethnopharmacol.* **2023**, *315*, 116641. [CrossRef] [PubMed]
48. Aliyu, Z.; Mahmud, A.D.; Oluwatoyin, A.B.; Aliyu, A.; Yahaya, A.S.; Saleh, A.M. Extraction and Characterization of Keratin Protein from Chicken Feathers using Alkaline Hydrolysis Method: Effects of Sodium Sulphide Concentration and Shelf-life Evaluation. *Malays. J. Catal.* **2023**, *7*, 37–41. [CrossRef]
49. Sun, Q.; Yu, L.; Zhang, Z.; Qian, C.; Fang, H.; Wang, J.; Wu, P.; Zhu, X.; Zhang, J.; Zhong, L.; et al. A novel gelatin/carboxymethyl chitosan/nano-hydroxyapatite/β-tricalcium phosphate biomimetic nanocomposite scaffold for bone tissue engineering applications. *Front. Chem.* **2022**, *10*, 958420. [CrossRef] [PubMed]
50. Thein-Han, W.; Misra, R. Biomimetic chitosan–nanohydroxyapatite composite scaffolds for bone tissue engineering. *Acta Biomater.* **2009**, *5*, 1182–1197. [CrossRef] [PubMed]
51. Bazgir, M.; Saeinasab, M.; Zhang, W.; Zhang, X.; Tsui, K.M.; Sarvestani, A.M.; Nawaz, S.; Coates, P.; Youseffi, M.; Elies, J.; et al. Investigation of Cell Adhesion and Cell Viability of the Endothelial and Fibroblast Cells on Electrospun PCL, PLGA and Coaxial Scaffolds for Production of Tissue Engineered Blood Vessel. *J. Funct. Biomater.* **2022**, *13*, 282. [CrossRef] [PubMed]
52. Suhaimi, H.; Das, D.B. Glucose diffusivity in cell-seeded tissue engineering scaffolds. *Biotechnol. Lett.* **2015**, *38*, 183–190. [CrossRef] [PubMed]
53. El-Bahrawy, N.R.; Elgharbawy, H.; Elmekawy, A.; Salem, M.; Morsy, R. Development of porous hydroxyapatite/PVA/gelatin/alginate hybrid flexible scaffolds with improved mechanical properties for bone tissue engineering. *Mater. Chem. Phys.* **2024**, *319*. [CrossRef]
54. Hernandez, A.M.; Santos, C.V.; De Icaza, M.; Castano, V. Microstructural characterisation of keratin fibres from chicken feathers. *Int. J. Environ. Pollut.* **2005**, *23*, 162–178. [CrossRef]
55. Senoz, E.; Wool, R.P. Microporous carbon-nitrogen fibers from keratin fibers by pyrolysis. *J. Appl. Polym. Sci.* **2010**, *118*, 1752–1765. [CrossRef]
56. Sharma, S.; Gupta, A.; Kumar, A.; Kee, C.G.; Kamyab, H.; Saufi, S.M. An efficient conversion of waste feather keratin into ecofriendly bioplastic film. *Clean Technol. Environ. Policy* **2018**, *20*, 2157–2167. [CrossRef]

57. Vasconcelos, A.; Freddi, G.; Cavaco-Paulo, A. Biodegradable materials based on silk fibroin and keratin. *Biomacromolecules* **2008**, *9*, 1299–1305. [CrossRef] [PubMed]
58. Silva, O.A.; Rossin, A.R.S.; Lima, A.M.d.O.; Valente, A.D.; Garcia, F.P.; Nakamura, C.V.; Follmann, H.D.M.; Silva, R.; Martins, A.F. Synthesis of Keratin Nanoparticles Extracted from Human Hair through Hydrolysis with Concentrated Sulfuric Acid: Characterization and Cytotoxicity. *Materials* **2024**, *17*, 3759. [CrossRef] [PubMed]
59. Das, M.P.; Suguna, P.R.; Prasad, K.; Vijaylakshmi, J.V.; Renuka, M. Extraction and Characterization of Gelatin: A Functional Biopolymer. *Int. J. Pharm. Pharm. Sci.* **2017**, *9*, 239. [CrossRef]
60. Padmanabhan, V.P.; Kulandaivelu, R.; Panneer, D.S.; Vivekananthan, S.; Sagadevan, S.; Lett, J.A. Microwave synthesis of hydroxyapatite encumbered with ascorbic acid intended for drug leaching studies. *Mater. Res. Innov.* **2019**, *24*, 171–178. [CrossRef]
61. Feughelman, M.; Lyman, D.; Willis, B. The parallel helices of the intermediate filaments of α-keratin. *Int. J. Biol. Macromol.* **2002**, *30*, 95–96. [CrossRef] [PubMed]
62. Xu, W.; Ke, G.; Wu, J.; Wang, X. Modification of wool fiber using steam explosion. *Eur. Polym. J.* **2006**, *42*, 2168–2173. [CrossRef]
63. Khosa, M.A.; Ullah, A. In-situ modification, regeneration, and application of keratin biopolymer for arsenic removal. *J. Hazard. Mater.* **2014**, *278*, 360–371. [CrossRef] [PubMed]
64. Poole, A.J.; Church, J.S. The effects of physical and chemical treatments on Na_2S produced feather keratin films. *Int. J. Biol. Macromol.* **2015**, *73*, 99–108. [CrossRef] [PubMed]
65. Mukasheva, F.; Adilova, L.; Dyussenbinov, A.; Yernaimanova, B.; Abilev, M.; Akilbekova, D. Optimizing scaffold pore size for tissue engineering: Insights across various tissue types. *Front. Bioeng. Biotechnol.* **2024**, *12*, 1444986. [CrossRef] [PubMed]
66. Balaji, S.; Kumar, R.; Sripriya, R.; Kakkar, P.; Ramesh, D.V.; Reddy, P.N.K.; Sehgal, P. Preparation and comparative characterization of keratin–chitosan and keratin–gelatin composite scaffolds for tissue engineering applications. *Mater. Sci. Eng. C* **2012**, *32*, 975–982. [CrossRef]
67. Hübner, C.; Vadalà, M.; Voges, K.; Lupascu, D.C. Poly(vinyl alcohol) freeze casts with nano-additives as potential thermal insulators. *Sci. Rep.* **2023**, *13*, 1020. [CrossRef] [PubMed]
68. Ko, Y.G. Formation of oriented fishbone-like pores in biodegradable polymer scaffolds using directional phase-separation processing. *Sci. Rep.* **2020**, *10*, 14472. [CrossRef] [PubMed]
69. Diaz, F.; Forsyth, N.; Boccaccini, A.R. Aligned Ice Templated Biomaterial Strategies for the Musculoskeletal System. *Adv. Healthc. Mater.* **2023**, *12*, e2203205. [CrossRef] [PubMed]
70. Kakkar, P.; Verma, S.; Manjubala, I.; Madhan, B. Development of keratin–chitosan–gelatin composite scaffold for soft tissue engineering. *Mater. Sci. Eng. C* **2014**, *45*, 343–347. [CrossRef] [PubMed]
71. Angulo, D.E.L.; Sobral, P.J.D.A. The effect of processing parameters and solid concentration on the microstructure and pore architecture of gelatin-chitosan scaffolds produced by freeze-drying. *Mater. Res.* **2016**, *19*, 839–845. [CrossRef]
72. Abbasi, N.; Hamlet, S.; Love, R.M.; Nguyen, N.-T. Porous scaffolds for bone regeneration. *J. Sci. Adv. Mater. Devices* **2020**, *5*, 1–9. [CrossRef]
73. Di Luca, A.; Ostrowska, B.; Lorenzo-Moldero, I.; Lepedda, A.; Swieszkowski, W.; Van Blitterswijk, C.; Moroni, L. Gradients in pore size enhance the osteogenic differentiation of human mesenchymal stromal cells in three-dimensional scaffolds. *Sci. Rep.* **2016**, *6*, 22898. [CrossRef] [PubMed]
74. Rasoulianboroujeni, M.; Kiaie, N.; Tabatabaei, F.S.; Yadegari, A.; Fahimipour, F.; Khoshroo, K.; Tayebi, L. Dual Porosity Protein-based Scaffolds with Enhanced Cell Infiltration and Proliferation. *Sci. Rep.* **2018**, *8*, 14889. [CrossRef] [PubMed]
75. Xiao, X.; Wang, W.; Liu, D.; Zhang, H.; Gao, P.; Geng, L.; Yuan, Y.; Lu, J.; Wang, Z. The promotion of angiogenesis induced by three-dimensional porous beta-tricalcium phosphate scaffold with different interconnection sizes via activation of PI3K/Akt pathways. *Sci. Rep.* **2015**, *5*, 9409. [CrossRef] [PubMed]
76. Mohamed, J.M.M.; Alqahtani, A.; Al Fatease, A.; Alqahtani, T.; Khan, B.A.; Ashmitha, B.; Vijaya, R. Human hair keratin composite scaffold: Characterisation and biocompatibility study on nih 3t3 fibroblast cells. *Pharmaceuticals* **2021**, *14*, 781. [CrossRef] [PubMed]
77. Kim, H.; Hwangbo, H.; Koo, Y.; Kim, G. Fabrication of mechanically reinforced gelatin/hydroxyapatite bio-composite scaffolds by core/shell nozzle printing for bone tissue engineering. *Int. J. Mol. Sci.* **2020**, *21*, 3401. [CrossRef] [PubMed]
78. Nayak, K.K.; Gupta, P. In vitro biocompatibility study of keratin/agar scaffold for tissue engineering. *Int. J. Biol. Macromol.* **2015**, *81*, 1–10. [CrossRef] [PubMed]
79. Razali, K.; Nasir, N.M.; Cheng, E.; Mamat, N.; Mazalan, M.; Wahab, Y.; Roslan, M.M. The effect of gelatin and hydroxyapatite ratios on the scaffolds′ porosity and mechanical properties. In Proceedings of the IECBES 2014, Conference Proceedings—2014 IEEE Conference on Biomedical Engineering and Sciences: "Miri, Where Engineering in Medicine and Biology and Humanity Meet", Sarawak, Malaysia, 8–10 December 2014; pp. 256–259. [CrossRef]
80. Lei, C.; Zhu, H.; Li, J.; Li, J.; Feng, X.; Chen, J. Preparation and characterization of polyhydroxybutyrate-co-hydroxyvalerate/silk fibroin nanofibrous scaffolds for skin tissue engineering. *Polym. Eng. Sci.* **2014**, *55*, 907–916. [CrossRef]

81. Jarząbek, D.M. The impact of weak interfacial bonding strength on mechanical properties of metal matrix – Ceramic reinforced composites. *Compos. Struct.* **2018**, *201*, 352–362. [CrossRef]
82. Lutzweiler, G.; Halili, A.N.; Vrana, N.E. The overview of porous, bioactive scaffolds as instructive biomaterials for tissue regeneration and their clinical translation. *Pharmaceutics* **2020**, *12*, 602. [CrossRef] [PubMed]
83. Raucci, M.G.; D'AMora, U.; Ronca, A.; Demitri, C.; Ambrosio, L. Bioactivation routes of gelatin-based scaffolds to enhance at nanoscale level bone tissue regeneration. *Front. Bioeng. Biotechnol.* **2019**, *7*, 27. [CrossRef] [PubMed]
84. Mahboudi, S.; Pezeshki-Modaress, M.; Noghabi, K.A. The study of fibroblast cell growth on the porous scaffold of gelatin-starch blend using the salt-leaching and lyophilization method. *Int. J. Polym. Mater. Polym. Biomater.* **2015**, *64*, 653–659. [CrossRef]
85. Rezwan, K.; Chen, Q.Z.; Blaker, J.J.; Boccaccini, A.R. Biodegradable and bioactive porous polymer/inorganic composite scaffolds for bone tissue engineering. *Biomaterials* **2006**, *27*, 3413–3431. [CrossRef] [PubMed]
86. Hong, S.-J.; Kim, D.-H.; Ryoo, J.-H.; Park, S.-M.; Kwon, H.-C.; Keum, D.-H.; Shin, D.-M.; Han, S.-G. Influence of Gelatin on Adhesion, Proliferation, and Adipogenic Differentiation of Adipose Tissue-Derived Stem Cells Cultured on Soy Protein–Agarose Scaffolds. *Foods* **2024**, *13*, 2247. [CrossRef] [PubMed]
87. Liu, W.; Cheong, N.; He, Z.; Zhang, T. Application of Hydroxyapatite Composites in Bone Tissue Engineering: A Review. *J. Funct. Biomater.* **2025**, *16*, 127. [CrossRef] [PubMed]
88. Aminatun; Sujak MK, A.; Izak R, D.; Hadi, S.; Sari, Y.W.; Gunawarman; Cahyati, N.; Yusuf, Y.; Abdullah, C.A.C. Fabrication and biocompatibility evaluation of hydroxyapatite-polycaprolactone-gelatin composite nanofibers as a bone scaffold. *RSC Adv.* **2024**, *14*, 24815–24827. [CrossRef] [PubMed]

Disclaimer/Publisher's Note: The statements, opinions and data contained in all publications are solely those of the individual author(s) and contributor(s) and not of MDPI and/or the editor(s). MDPI and/or the editor(s) disclaim responsibility for any injury to people or property resulting from any ideas, methods, instructions or products referred to in the content.